Journal of Computational Physics 229 (2010) 561–593

Contents lists available at ScienceDirect

Journal of Computational Physics

journal homepage: www.elsevier.com/locate/jcp

High-order sonic boom modeling based on adaptive methods

F. Alauzet *, A. Loseille

INRIA, Projet Gamma, Domaine de Voluceau, Rocquencourt, BP 105, 78153 Le Chesnay Cedex, France

ARTICLE INFO

Article history:
Received 27 March 2009
Received in revised form 11 September 2009
Accepted 17 September 2009
Available online 9 October 2009

Keywords:
Sonic boom
Euler equations
Finite volume
Anisotropic mesh adaptation
Waveform parameter method

ABSTRACT

This paper presents an accurate approach to simulate the sonic boom of supersonic aircrafts. The near-field flow is modeled by the conservative Euler equations and is solved using a vertex-centered finite volume approach on adapted unstructured tetrahedral meshes. A metric-based anisotropic mesh adaptation is considered to control the interpolation error in L^p norm. Then, from the CFD solution, the pressure distribution under the aircraft is extracted and used to set up the initial conditions of the propagation algorithm in the far-field. The pressure distribution is propagated down to the ground in order to obtain the sonic boom signature using a ray tracing algorithm based upon the Thomas waveform parameter method. In this study, a sonic boom sensitivity analysis is carried out on several aircraft designs (low-drag and low-boom shapes).

© 2009 Elsevier Inc. All rights reserved.

1. Introduction

Sonic boom, like every sound, corresponds to a small variation (positive for a compression or negative for an expansion) of the ambient air pressure with respect to the atmospheric pressure. This acoustic phenomenon is associated with bodies moving in atmosphere at a speed exceeding the local speed of sound. When an aircraft exceeds the speed of sound, shock waves are generated at its surface and emanate outward, forming the Mach cone. Usually, these shock waves coalesce into a characteristic N shape wave when they propagate in atmosphere toward the ground. The "boom–boom" heard on the ground comes from the abrupt pressure increase in the ambient air, *i.e.,* the two shock waves of the *N* shape acoustic signal. The region exposed to the sonic boom horizontally extends on each side of the aircraft path on the ground on a band of 60 to 80 km width depending on the flight conditions, see Fig. 1. As a result, the sonic boom of supersonic aircrafts has a major impact on the environment: annoyance for the population due to noise and startle, but also rattles and vibrations on buildings. At worst, the latter phenomenon can break windows and damage buildings. For this reason, the most of current national regulation does not allow any supersonic flight over land. For instance, Concorde, that flew from 1969 to 2003, was allowed to fly supersonically only over water because its boom annoyed people on the ground.

Nonetheless, there is nowadays a substantial economic interest in designing a low sonic boom supersonic business jet that respects this environmental constraint. Indeed, if we consider a flight above the US from New York to Los Angeles, the travel time can be divided by two while flying at a supersonic cruise speed instead of a subsonic one. There is no conventional shape to reduce the boom, this is the main problem. However, it has been stated [29] that a significant reduction in shock overpressure levels is achieved by reducing the jet size, *i.e.,* its weight. Consequently, focussing on business jets would be the first step. Several companies all around the world are thus involved in several research programs in order to propose low boom shape supersonic business jets (SSBJs).

* Corresponding author. Tel.: +33 1 39 63 57 93; fax: +33 1 39 63 58 82.
E-mail address: Frederic.Alauzet@inria.fr (F. Alauzet).

0021-9991/$ - see front matter © 2009 Elsevier Inc. All rights reserved.
doi:10.1016/j.jcp.2009.09.020

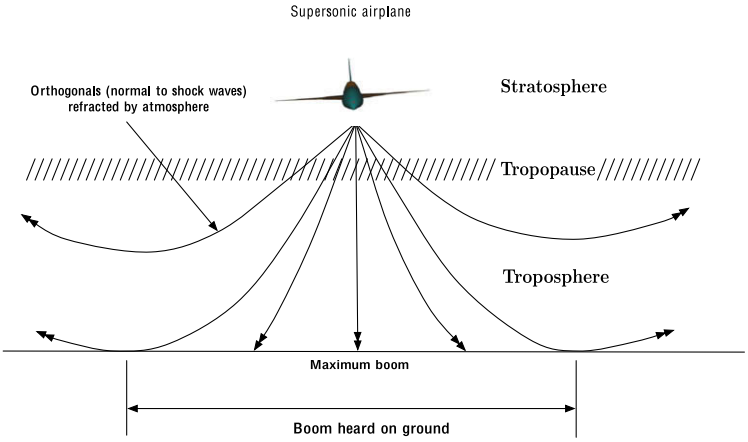

Fig. 1. Illustration of the sonic boom horizontal carpet with under the aircraft path and the refraction of acoustic waves by atmosphere.

In this context, numerical simulation faces a challenging problem. As constructing prototype is very (too) expensive, numerical simulation, coupled with wind-tunnel testing, is currently the main way to design low boom aircraft shapes. To this end, shape optimization methods, that are now mature, are employed. But, an optimization process will converge toward the best low boom shape only if the sensitivity function is accurately evaluated. Therefore, numerical methods must have the ability to assess the computed sonic boom for a given shape. It ensures that the direction of the gradient descent is not due to numerical artifacts. High-fidelity numerical predictions of the sonic boom are thus of main interest in designing low sonic boom aircraft configurations.

1.1. Modeling the sonic boom

The main difficulty in high-fidelity sonic boom numerical modeling lies in the large variations of the problem scales: they vary from millimeter on the aircraft to kilometer in atmosphere. But nowadays, considering the ever-increasing computational power available, such high-fidelity predictions become conceivable. Indeed, fairly simple methods based on linear theories were used in the past to predict sonic booms, such as [4]. Today, methods coupling CFD, that enable accurate non-linear near-field solutions around aircrafts, with linear acoustics for propagation in atmosphere toward the ground are available [27,30]. More precisely, the flow close to the aircraft, called aerodynamic near-field region, is computed by solving the conservative Euler equations for gas dynamic. Then, from the CFD solution, the pressure distribution under the aircraft is extracted and used to set up the initial conditions for the propagation algorithm in the far-field. The pressure distribution is then propagated down to the ground to compute the sonic boom signature using linear acoustics.

The main problematic with these coupled methods is that some assumptions are required to ensure a valid coupling. As stated in [30], there is a matching radius between the source function and the propagation extrapolation. The assumption is that the use of the pressure signal becomes valid when the flow field does not contain crossflow components anymore. As crossflow components are very significant at small radii but are less at larger distances, the pressure signal has to be extracted in the mid-field far enough from the aircraft to respect such a condition. This is a necessary condition to take all the elements of the aircraft geometry (body, wings, engine, etc.) into account.

1.2. Present status

Standard CFD on unstructured meshes is only able to attain at most a one-aircraft-length distance below the jet which is not enough to validate the coupling for complex geometries. After this distance, the solution is completely dissipated and the signal is lost. Consequently, new three-stage methods have been developed. One method considers a coupling between CFD, a multi-pole based near-field reconstruction to take into account crossflow components [13] and linear propagation [31]. Another approach couples near-field, mid-field and far-field simulations, see for instance [38]. However, these methods still involve CFD computations that have to be accurate to provide correct sonic boom predictions. Indeed, these CFD computations generally employ isotropic unstructured meshes (to be able to handle complex aircraft geometries) leading to a lot of numerical dissipation while propagating the shock waves. Thus, certified CFD computation seems to be a necessity.

Besides, in the last decade, 3D meshing dedicated to CFD has tremendously progressed with notably the advent of anisotropic mesh adaptation. This technique has already proved its efficiency to reduce drastically the required number of degrees of freedom to achieve a given complexity [6,11,15,23,28,36]. Furthermore, anisotropic mesh adaptation particularly reduces the numerical dissipation of shock capturing schemes and recovers the numerical scheme convergence order that is

generally lost for flows with genuine discontinuities [26]. In this paper, we propose an alternative two-stage approach based on adaptive CFD.

1.3. The proposed approach

A high-fidelity method to accurately predict the sonic boom emitted by supersonic aircrafts is discussed. This approach is fully automatic and thus immediately applicable whatever the aircraft geometry and whatever the flight conditions. It aims at:

- Controlling the impact of the numerical dissipation of flow solvers on unstructured meshes. The intensity of shocks is preserved while they propagate through the domain, along with the non-linearities of the solution.
- Computing accurate CFD mid-field signature, *i.e.,* the pressure signature at a distance of the order of the kilometer from the aircraft. In particular, shock waves are kept separated in the mid-field and do not merge artificially due to any coarse mesh effect.

In our high-fidelity model, the resolution is two stepped, see Fig. 2. Near-field and mid-field flows are solved using a vertex-centered finite volume approach on anisotropic adapted unstructured tetrahedral meshes. Adapted anisotropic meshes are utilized to break scale factors, leading to accurate near-field and mid-field predictions [11,26]. The pressure distribution is then propagated down to the ground to compute the sonic boom signature using a ray tracing algorithm based upon the Thomas waveform parameter method [37].

As regards CPU time, this strategy can lead to fast answers or to large CFD computations depending on the study criteria. For calculations of mid-field pressure signals at small distances (100 m) without convergence analysis, computations are achieved in a couple of hours on eight 2.8 GHz Intel processors. On the opposite, for large distance mid-field pressure signal computations (the order of the kilometer) with convergence analysis in order to assess sonic boom prediction, simulations necessitate dozens of millions of degrees of freedom for the last adapted mesh, which results in one week simulations on eight processors.

In the present work, attention is paid to the coupling between mid-field resolution and far-field propagation. To resolve this issue, a convergence study of sonic boom signatures with respect to extraction distances for the whole adaptive process is carried out.

In addition to the validity of the coupling, we aim at assessing the obtained numerical results as much as possible. We would like to attest that the computed mid-field signature and the sonic boom signal converge toward the physical solution. In this paper, we show that anisotropic mesh adaptation helps to answer this question. Indeed, in order to be able to certify a result, the mesh convergence order of the numerical solution must be equal to the theoretical order of the numerical scheme. However, global second order of mesh convergence is generally scarcely reached for most practical applications in which genuine discontinuities or sharp gradients are involved – and it is the case for the sonic boom problem. It has been demonstrated in [26] that anisotropic mesh adaptation enables to recover the theoretical convergence order. In broad outline, the

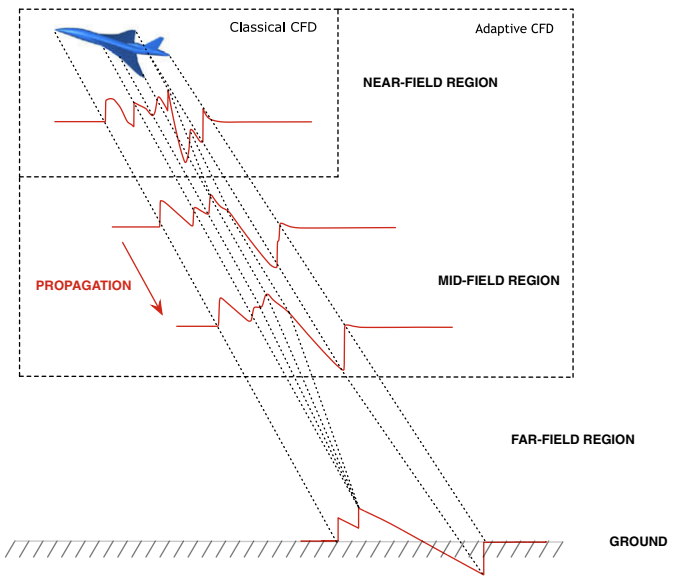

Fig. 2. Sonic boom problem modeling.

mesh adaptation strategy automatically asks the mesh generator to set the adequate number of required vertices in all regions to attain the theoretical convergence order.

1.4. Overview

Section 2 details the CFD modeling. Section 2.1 describes the vertex-centered finite volume scheme used to compute near-field and mid-field regions flows and Section 2.2 recalls the mesh adaptation algorithm. We briefly review the main stages of the adaptation procedure. The CFD part is validated in Section 2.3 by comparison to experimental data. Then in Section 3, the ray tracing algorithm based upon the Thomas waveform parameter method is recalled and the coupling between the CFD and the propagation code is clarified. Finally, in Section 4, several aircraft shapes, provided by Dassault Aviation in the HISAC European project, are analyzed and compared. We eventually point out the impact of anisotropic mesh adaptation to compute accurate mid-field signatures with CFD.

2. CFD modeling

The near-field flow around the aircraft is modeled by the conservative Euler equations. Assuming that the gas is perfect, inviscid and that there is no thermal diffusion, the Euler equations for mass, momentum and energy conservation read:

$$\begin{cases} \frac{\partial \rho}{\partial t} + \nabla \cdot (\rho \mathbf{U}) = 0, \\ \frac{\partial (\rho \mathbf{U})}{\partial t} + \nabla \cdot (\rho \mathbf{U} \otimes \mathbf{U}) + \nabla p = 0, \\ \frac{\partial (\rho E)}{\partial t} + \nabla \cdot ((\rho E + p)\mathbf{U}) = 0, \end{cases}$$

where ρ denotes the density, $\mathbf{U}$ the velocity vector, $E = T + \frac{\|\mathbf{U}\|^2}{2}$ the total energy and $p = (\gamma - 1)\rho T$ the pressure with $\gamma = 1.4$ the ratio of specific heats and T the temperature. These equations can be rewritten:

$$\frac{\partial W}{\partial t} + \nabla \cdot F(W) = 0, \tag{1}$$

where $W = {}^t(\rho, \rho\mathbf{U}, \rho E)$ is the conservative variables vector and the matrix F represents the convective operator.

The Euler system is solved with a finite volume technique on unstructured tetrahedral meshes using `Wolf`, a in-house flow solver. The resolution is performed on highly anisotropic adapted meshes to enhance drastically the simulation accuracy. This is a (the only) way to propagate Mach cone emitted by the aircraft several kilometers below in the mid-field. The flow solver and the mesh adaptation methods are presented in the following sections. A last section validates the approach on two test cases experimented at NASA [5,19].

2.1. Flow solver

The proposed method is a vertex-centred finite volume scheme applied to tetrahedral unstructured meshes which uses a particular edge-based formulation with upwind elements introduced in [9]. This flow solver employs the HLLC or the Roe approximate Riemann solver to compute numerical fluxes. High-order scheme is derived according to a MUSCL (Monotone Upwind Schemes for Conservation Laws) type method using downstream and upstream tetrahedra. This approach is compatible with vertex-centered and edge-based formulations. Consequently, an inexpensive high-order extension of monotone upwind schemes is easily derived. The flux integration based on the edges and their corresponding upwind elements

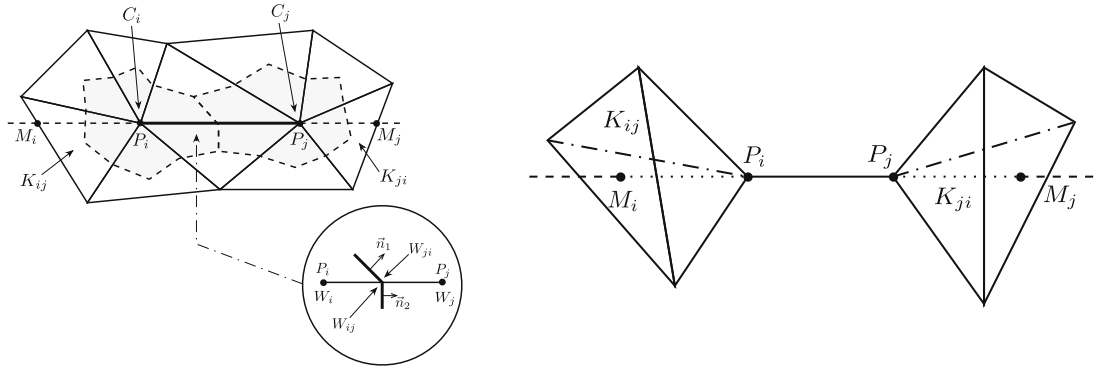

Fig. 3. Left, illustration of finite volume cells construction in 2D with two neighboring cells C_i and C_j, and the upwind triangles K_{ij} and K_{ji} associated with edge P_iP_j. The common boundary ∂C_{ij} with the representation of the solution extrapolated values for the MUSCL type approach is shown. Right, downstream K_{ij} and upstream K_{ji} tetrahedra associated with edge P_iP_j.

(crossed by the edge) is a key-feature in order to preserve the positivity of the density for vertex-centered formulation. The MUSCL type method is combined with a generalization of the Superbee limiter with three entries to guarantee the TVD (Total Variation Diminishing) property of the scheme. An explicit time stepping algorithm is used by means of a strong–stability–preserving (SSP) Runge–Kutta scheme.

2.1.1. Scheme for convective fluxes

The vertex-centered finite volume formulation consists in associating with each vertex P_i of the mesh a control volume or finite volume cell, denoted C_i. The dual finite volume cell mesh is built by the rule of medians. The common boundary $\partial C_{ij} = \partial C_i \cap \partial C_j$ between two neighboring cells C_i and C_j is decomposed in several triangular interface facets. An illustration of this construction in two dimensions is shown in Fig. 3.

Hence applying the finite volume method to the Euler equations, we get for each finite volume cell C_i:

$$|C_i|\frac{dW_i}{dt} + \int_{\partial C_i} F(W_i)\cdot \mathbf{n}_i \, d\gamma = 0, \tag{2}$$

where W_i is the mean value of the solution W on the cell C_i and $\mathbf{n}_i$ is the outer normal to the cell C_i. The integration of the convective fluxes F is done by decomposing the cell boundary in facets ∂C_{ij}:

$$\int_{\partial C_i} F(W_i)\cdot \mathbf{n}_i \, d\gamma = \sum_{P_j \in \mathcal{V}(P_i)} F|_{l_{ij}} \cdot \int_{\partial C_{ij}} \mathbf{n}_i \, d\gamma,$$

where $\mathcal{V}(P_i)$ is the set of all neighboring vertices of P_i and $F|_{l_{ij}}$ represents the constant value of $F(W)$ at the interface ∂C_{ij}.

The flow is calculated with a numerical flux function, denoted Φ_{ij}:

$$\Phi_{ij} = \Phi_{ij}(W_i, W_j, \mathbf{n}_{ij}) = F|_{l_{ij}} \cdot \int_{\partial C_{ij}} \mathbf{n}_i \, d\gamma, \tag{3}$$

where $\mathbf{n}_{ij} = \int_{\partial C_{ij}} \mathbf{n}_i \, d\gamma$. The numerical flux function approximates the hyperbolic terms on the common boundary ∂C_{ij}. We notice that the computation of the convective fluxes is performed mono-dimensionaly in the direction normal to the boundary of the finite volume cell. Therefore, the numerical calculation of the flux function Φ_{ij} at the interface ∂C_{ij} is achieved by the resolution of a one-dimensional Riemann problem in the direction of the normal $\mathbf{n}_{ij}$ by means of an approximate Riemann solver.

Several upwind numerical flux functions are available and can be formally written:

$$\Phi_{ij}(W_i, W_j, \mathbf{n}_{ij}) = \frac{F(W_i)+F(W_j)}{2}\cdot \mathbf{n}_{ij} + d(W_i, W_j, \mathbf{n}_{ij}), \tag{4}$$

where the function $d(W_i, W_j, \mathbf{n}_{ij})$ contains the upwind terms and depends on the chosen scheme. In this paper, we compare the Roe and the HLLC approximate Riemann solver that we summarize below. More details on Roe and HLLC solvers are found in [32,3], respectively.

2.1.1.1. Roe approximate Riemann solver. In the Roe approach, the upwinding term d is defined by the Jacobian matrix of F:

$$A(W) = \frac{\partial (F(W)\cdot \mathbf{n}_{ij})}{\partial W}.$$

The eigenvalues of $A(W)$ are real and given by $u, u+c$ and $u-c$. In the context of the Euler equations, the hyperbolic flux is homogeneous of order one leading to the property:

$$F(W)\cdot \mathbf{n}_{ij} = A(W)W,$$

that enables non-oscillatory conservative schemes to be built. The flux resolution uses the formulation of Φ introduced by Roe:

$$\Phi^{\mathrm{Roe}}(W_i, W_j, \mathbf{n}_{ij}) = \frac{F(W_i)+F(W_j)}{2}\cdot \mathbf{n}_{ij} + |\widetilde{A}(W_i, W_j)|\frac{W_i - W_j}{2},$$

where $\widetilde{A}$ is the Jacobian of F evaluated for the Roe average variables and for a diagonalizable matrix $A = P\Lambda P^{-1}$ we have denoted $|A| = P|\Lambda|P^{-1}$. Let W_l and W_r be the two states, then the Roe averages are given by:

$$\tilde{\rho} = \sqrt{\rho_l \rho_r}, \quad \widetilde{\mathbf{U}} = \frac{\sqrt{\rho_l}\mathbf{U}_l + \sqrt{\rho_r}\mathbf{U}_r}{\sqrt{\rho_l}+\sqrt{\rho_r}} \quad \text{and} \quad \widetilde{H} = \frac{\sqrt{\rho_l}H_l + \sqrt{\rho_r}H_r}{\sqrt{\rho_l}+\sqrt{\rho_r}}$$

from which we get Roe average sound speed: $\tilde{c}^2 = (\gamma-1)\left(\widetilde{H} - \frac{1}{2}\tilde{q}^2\right)$ where $\tilde{q}^2 = \|\widetilde{\mathbf{U}}\|^2$.

2.1.1.2. HLLC approximate Riemann solver. The idea of the HLLC solver is to consider locally a simplified Riemann problem with two intermediate states depending on the local left and right states. The simplified solution to the Riemann problem consists of a contact wave with a velocity S_M and of two acoustic waves, which may be either shocks or expansion fans.

The acoustic waves have the smallest and the largest velocities (S_L and S_R, respectively) of all the waves present in the exact solution. If $S_L > 0$ then the flow is supersonic from left to right and the upwind flux is simply defined from $F(W_l)$ where W_l is the state on the left of the discontinuity. Similarly, if $S_R < 0$ then the flow is supersonic from right to left and the flux is determined by $F(W_r)$ where W_r is the state on the right of the discontinuity. In the more difficult subsonic case when $S_L < 0 < S_R$ we have to calculate $F(W_l^*)$ or $F(W_r^*)$. Consequently, the HLLC flux is given by:

$$\Phi^{\mathrm{HLLC}} = \begin{cases} F_l & \text{if } S_L > 0, \\ F_l^* & \text{if } S_L \leqslant 0 < S_M, \\ F_r^* & \text{if } S_M \leqslant 0 \leqslant S_R, \\ F_r & \text{if } S_R < 0. \end{cases}$$

Now, let us specify how W_l^* and W_r^* are evaluated. We denote by $\eta = \mathbf{U}.\mathbf{n}$. In [3], the following evaluation is proposed:

$$F_l^* = F_l + S_L(W_l^* - W_l),$$
$$F_r^* = F_r + S_R(W_r^* - W_r),$$

from which the W_l^* and W_r^* are computed. Assuming that $\eta^* = \eta_l^* = \eta_r^* = S_M$, we obtain (the subscript l or r are omitted for clarity)

$$W^* = \frac{1}{S - S_M}\begin{pmatrix} \rho(S-\eta) \\ \rho\mathbf{U}(S-\eta) + (p^* - p)\mathbf{n} \\ \rho E(S-\eta) + p^* S_M - p\eta \end{pmatrix} = \frac{1}{S - \eta^*}\begin{pmatrix} \rho(S-\eta) \\ \rho\mathbf{U}(S-\eta) + (p^* - p)\mathbf{n} \\ \rho E(S-\eta) + p^* \eta^* - p\eta \end{pmatrix},$$

where

$$p^* = \rho(S-\eta)(S_M - \eta) + p.$$

The key of this solver lies in the definition of the three waves velocity. For the contact wave, the following velocity is considered:

$$S_M = \frac{\rho_r \eta_r (S_R - \eta_r) - \rho_l \eta_l (S_L - \eta_l) + p_l - p_r}{\rho_r (S_R - \eta_r) - \rho_l (S_L - \eta_l)},$$

and the other acoustic wave speeds are based on the Roe averages:

$$S_L = \min(\eta_l - c_l, \tilde{\eta} - \tilde{c}) \quad \text{and} \quad S_R = \max(\eta_r + c_r, \tilde{\eta} + \tilde{c}).$$

With such waves velocities, the HLLC approximate Riemlann solver has the following properties. It automatically: (i) satisfies the entropy inequality, (ii) resolves isolated contacts exactly, (iii) resolves isolated shocks exactly and (iv) preserves positivity.

Such a formulation gives at best only a first-order scheme, higher-order extensions are possible with a MUSCL type technique.

2.1.2. High-order accurate version

The MUSCL type reconstruction method has been designed to increase the order of accuracy of the scheme. This method was introduced by Van Leer in a series of papers, see for instance [22]. The idea is to use extrapolated values W_{ij} and W_{ji} of W at the interface ∂C_{ij} to evaluate the flux, cf. Fig. 3 left. The following approximation is performed:

$$\Phi_{ij} = \Phi_{ij}(W_{ij}, W_{ji}, \mathbf{n}_{ij}),$$

with W_{ij} and W_{ji} which are linearly interpolated as:

$$\begin{cases} W_{ij} = W_i + \frac{1}{2}(\nabla W)_{ij} \cdot \vec{P_i P_j}, \\ W_{ji} = W_j + \frac{1}{2}(\nabla W)_{ji} \cdot \vec{P_j P_i}, \end{cases} \tag{5}$$

where, in contrast to the original MUSCL approach, the approximate "slopes" $(\nabla W)_{ij}$ and $(\nabla W)_{ji}$ are defined for any edge and obtained using a combination of centered, upwind and nodal gradients.

The centered gradient, which is related to edge P_iP_j, is defined as:

$$(\nabla W)_{ij}^C \cdot \overrightarrow{P_i P_j} = W_j - W_i.$$

Upwind and downwind gradients, which are also related to edge P_iP_j, are computed according to the definition of upstream and downstream tetrahedra of edge P_iP_j. These tetrahedra are respectively denoted K_{ij} and K_{ji}, cf. Fig. 3 right. K_{ij} (resp. K_{ji}) is the unique tetrahedron of the ball of P_i (resp. P_j) the opposite face of which is crossed by the line defined by the edge P_iP_j.

Upwind and downwind gradients are then defined for vertices P_i and P_j as:

$$(\nabla W)_{ij}^{U} = (\nabla W)|_{K_{ij}} \quad \text{and} \quad (\nabla W)_{ij}^{D} = (\nabla W)|_{K_{ji}}.$$

where $(\nabla W)|_K = \sum_{P\in K} W_P \nabla\phi_P|_K$ is the P_1-Galerkin gradient on tetrahedron K. Parametrized nodal gradients are built by introducing the β-scheme:

$$(\nabla W)_{ij} = (1-\beta)(\nabla W)_{ij}^{C} + \beta(\nabla W)_{ij}^{U},$$
$$(\nabla W)_{ji} = (1-\beta)(\nabla W)_{ij}^{C} + \beta(\nabla W)_{ij}^{D},$$

where $\beta \in [0,1]$ is a parameter controlling the amount of upwinding. For instance, the scheme is centered for $\beta = 0$ and fully upwind for $\beta = 1$.

2.1.2.1. Numerical dissipation of fourth-order: V4-scheme. The most accurate β-scheme is obtained for $\beta = 1/3$. Indeed, it can be demonstrated that this scheme is third-order for the two-dimensional linear advection on structured triangular meshes. In our case, for the non-linear Euler equations on unstructured meshes, a second-order scheme with a fourth-order numerical dissipation is obtained. These high-order gradients are given by:

$$(\nabla W)_{ij}^{V4} = \frac{2}{3}(\nabla W)_{ij}^{C} + \frac{1}{3}(\nabla W)_{ij}^{U},$$
$$(\nabla W)_{ji}^{V4} = \frac{2}{3}(\nabla W)_{ji}^{C} + \frac{1}{3}(\nabla W)_{ij}^{D}.$$

2.1.2.2. Numerical dissipation of sixth-order: V6-scheme. An even less dissipative scheme has been proposed in [9]. It is a more complex linear combination of gradients using centered, upwind and nodal P_1-Galerkin gradients. The nodal P_1-Galerkin gradient of P_i is related to cell C_i and is computed by averaging the gradients of all the tetrahedra containing vertex P_i:

$$(\nabla W)_{P_i} = \frac{1}{4|C_i|}\sum_{K\in C_i} |K|(\nabla W)|_K.$$

A sixth-order dissipation scheme is then obtained by considering the following high-order gradient:

$$(\nabla W)_{ij}^{V6} = (\nabla W)_{ij}^{V4} - \frac{1}{30}\left((\nabla W)_{ij}^{U} - 2(\nabla W)_{ij}^{C} + (\nabla W)_{ij}^{D}\right) - \frac{2}{15}\left((\nabla W)_{M_i} - 2(\nabla W)_{P_i} + (\nabla W)_{P_j}\right),$$
$$(\nabla W)_{ji}^{V6} = (\nabla W)_{ji}^{V4} - \frac{1}{30}\left((\nabla W)_{ij}^{D} - 2(\nabla W)_{ij}^{C} + (\nabla W)_{ij}^{U}\right) - \frac{2}{15}((\nabla W)_{M_j} - 2(\nabla W)_{P_j} + (\nabla W)_{P_i}),$$

where $(\nabla W)_{M_{i,j}}$ is the gradient at the points $M_{i,j}$ intersection of the line defined by P_iP_j and upwind–downwind tetrahedra, see Fig. 3 right. These gradients are computed by linear interpolation of the vertices attached nodal gradients of face containing $M_{i,j}$.

2.1.2.3. Dervieux limiter. The previous MUSCL schemes are not monotone. Therefore, limiting functions must be coupled with the previous high-order gradient evaluations to guarantee the TVD property of the scheme. The gradient of Relation (5) is substituted by a limited gradient denoted $(\nabla W)_{ij}^{\lim}$. Here, we consider the three-entries limiter introduced by Dervieux which is a generalization of the Superbee limiter [8]:

if $uv \leqslant 0$ then
  $Lim(u,v,w) = 0$
else
  $Lim(u,v,w) = Sign(u)min(2|u|, 2|v|, |w|)$,

and we use: $Lim\left((\nabla W)_{ij}^{C}, (\nabla W)_{ij}^{D}, (\nabla W)_{ij}^{HO}\right)$ where $(\nabla W)_{ij}^{HO}$ is even $(\nabla W)_{ij}^{V4}$ or $(\nabla W)_{ij}^{V6}$.

2.1.3. Boundary conditions

For aircraft supersonic flow simulations, three boundary conditions are required. Slip boundary conditions are imposed for the body as the flow is considered inviscid. We used Steger–Warming flux [35] to set up free-stream (external flow) conditions. And finally, for geometries with engines, the inlet and the exhaust are modeled with a modified Steger–Warming flux.

2.1.3.1. Slip condition. For this boundary condition we impose weakly

$$\mathbf{U}\cdot\mathbf{n} = 0. \tag{6}$$

To this end, we compute the flux Φ between the state on the boundary W and a mirror state $\overline{W}$:

$$W = \begin{pmatrix} \rho \\ \rho \mathbf{U} \\ \rho E \end{pmatrix} \quad \text{and} \quad \overline{W} = \begin{pmatrix} \rho \\ \rho \mathbf{U} - 2\rho(\mathbf{U}\cdot\mathbf{n})\mathbf{n} \\ \rho E \end{pmatrix}.$$

If Condition (6) is verified then $W = \overline{W}$ and thus $\Phi(W,\overline{W}) = F(W)$. Moreover, as W verifies Relation (6), $F(W)$ simplifies to:

$$\Phi_{\text{Slip}} = F(W) = (0, p\mathbf{n}, 0)^t.$$

Therefore, if the desired condition is satisfied, then the boundary flux reduced to its well known commonly used form.

Nevertheless, the state W on the boundary does not satisfy this condition unless it is imposed strongly which is not possible as we will no more conserve the mass. This problem is solved by computing the flux between the state and its mirror state. This flux depends on the considered flux. Let us presents the Roe and the HLLC versions.

2.1.3.2. Roe flux. By definition, we have $c = \bar{c}, p = \bar{p}$ and $H = \overline{H}$. Notably, we get $\mathbf{U}\cdot\mathbf{n} = -\overline{\mathbf{U}}\cdot\mathbf{n}$. In this particular case, the Roe averages simplify to

$$\tilde{\rho} = \rho, \quad \widetilde{\mathbf{U}} = \mathbf{U} - (\mathbf{U}\cdot\mathbf{n})\mathbf{n} = \mathbf{U_t} \quad \text{and} \quad \tilde{H} = H,$$

where $\mathbf{U}_t$ is the velocity in the tangent plane. We deduce:

$$\widetilde{\mathbf{U}}\cdot\mathbf{n} = 0, \quad \tilde{q}^2 = \|\mathbf{U_t}\|^2 = q^2 - (\mathbf{U}\cdot\mathbf{n})^2 \quad \text{and} \quad \tilde{c}^2 = (\gamma-1)\left(H - \frac{1}{2}\tilde{q}^2\right).$$

Notice that the Roe averages verify the slipping condition: $\widetilde{\mathbf{U}}\cdot\mathbf{n} = 0$. Computing analytically the Roe flux leads to:

$$\Phi_{\text{Slip}} = \Phi^{\text{Roe}}(W,\overline{W},\mathbf{n}) = (0, (p + \rho\tilde{c}(\mathbf{U}\cdot\mathbf{n}) + \rho(\mathbf{U}\cdot\mathbf{n})^2)\mathbf{n}, 0)^t.$$

This flux can be written shortly: $\Phi^{\text{Roe}}(W,\overline{W},\mathbf{n}) = (0, p^\star\mathbf{n}, 0)^t$.

2.1.3.3. HLLC flux. To compute Φ^{HLLC} we still have to evaluate the Roe averages to define the waves speed. The left and right waves speed are then given by

$$S_L = \min(\mathbf{U}\cdot\mathbf{n} - c, -\tilde{c}) \quad \text{and} \quad S_R = \max(-\mathbf{U}\cdot\mathbf{n} + c, \tilde{c}).$$

Therefore, we always have $S_L < 0$ and $S_R > 0$, as $\tilde{c} > 0$. The flux is then given by one of the intermediate state W^*. But in this case, it simplifies again:

$$S^* = 0 = \mathbf{U}^*\cdot\mathbf{n},$$

as $S_L + S_R = 0$ meaning that the intermediate state verifies the slipping condition. Finally, we get:

$$\Phi_{\text{Slip}} = \Phi^{\text{HLLC}}(W,\overline{W},\mathbf{n}) = F(W^*) = (0, p^*\mathbf{n}, 0)^t,$$

with $p^* = p + \rho\mathbf{U}\cdot\mathbf{n}(\mathbf{U}\cdot\mathbf{n} - S_L) = p + \rho\mathbf{U}\cdot\mathbf{n}\min(c, \tilde{c} + \mathbf{U}\cdot\mathbf{n})$.

Let us give two remarks about the proposed slip condition. If the wave speed is defined by the Roe averages in the HLLC flux then we have $p^* = p^\star$ and thus $\Phi^{\text{HLLC}} = \Phi^{\text{Roe}}$ which is consistent. Moreover, if Condition (6) is verified, we get $p = p^\star = p^*$ and the computed flux become the usual one. The added term to the pressure acts as a correction term to take into account the violation of Condition (6) by the current state.

2.1.3.4. Free-stream condition. This condition imposes a free-stream uniform flow from the infinite. It applies when we have a boundary Γ_∞ for which the infinite constant state W_∞ is known. We assume that the infinite state is uniform:

$$W_\infty = \begin{pmatrix} \rho_\infty \\ (\rho\mathbf{U})_\infty \\ (\rho E)_\infty \end{pmatrix}.$$

This state enables upwind fluxes at the infinite to be computed. The considered boundary fluxes are built from a decomposition following the characteristics values. We consider the Steger–Warming flux [35] which is completely upwind on the solution W_i:

$$\Phi_\infty = A^+(W_i,\mathbf{n_i})W_i + A^-(W_i,\mathbf{n_i})W_\infty,$$

where $A^+ = \frac{|A|+A}{2}$ and $A^- = \frac{|A|-A}{2}$.

2.1.3.5. Engine condition. Engines boundary conditions are defined by a given number of variables representing the engine data. All variables are linked by the isentropic relations that in particular connects the static state to the total state. These data are used to define the jet state W_{jet}. To set up the engine data, the flow solver requires:

- Three data for the inlet: $M^{\text{in}}, p_s^{\text{in}}$ and T_t^{in}.
- Three data for the exhaust: $M^{\text{out}}, p_t^{\text{out}}$ and T_t^{out}.

where subscript ^{s} and ^{t} denote the static and the total variables, respectively. Moreover, the direction of the flow is considered normal to the inlet or exhaust face: $\mathbf{U} = \|\mathbf{U}\|\mathbf{n}$. The flux is computed using a modified Steger and Warming boundary condition for inlet and exhaust:

$$\Phi_{\text{jet}} = A^+(W_{\text{jet}}, \mathbf{n_i})W_i + A^-(W_{\text{jet}}, \mathbf{n_i})W_{\text{jet}},$$

where W_{jet} and W_i are the engine constant state and the local vertex state, respectively.

2.1.4. Time advancing

An explicit scheme is used to advance the Euler equations in time by a line method, *i.e.,* time and space are treated separately. Once the equations have been discretized in space, a set of ordinary differential equations in time is obtained: $W_t - L(W) = 0$. To discretize the previous relation, a high-order multi-step Runge–Kutta scheme is considered. Such time discretization methods, called SSP (strong–stability–preserving), have non-linear stability properties which are particularly suitable for the integration of system of hyperbolic conservation laws where discontinuities appear. These schemes verify the TVD property.

The optimal 2-stage order-2 SSP Runge–Kutta scheme introduced by Shu and Osher [33] is the following modified Euler scheme:

$$\begin{aligned} W^{(1)} &= W^n + \Delta t L(W^n), \\ W^{n+1} &= \frac{1}{2}W^n + \frac{1}{2}W^{(1)} + \frac{1}{2}\Delta t L(W^{(1)}), \end{aligned}$$

which accept to use a *CFL* coefficient up to 1. In this study, we consider a 5-stage order-2 SSPRK scheme given in [34] that enables us to consider *CFL* coefficient up to 4. This scheme reads:

$$\begin{aligned} W^{(1)} &= W^n + \frac{1}{4}\Delta t L(W^n), \\ W^{(k)} &= W^{(k-1)} + \frac{1}{4}\Delta t L(W^{(k-1)}), \quad k = 2, \ldots, 4, \\ W^{n+1} &= \frac{1}{5}W^n + \frac{4}{5}W^{(4)} + \frac{1}{5}\Delta t L(W^{(4)}). \end{aligned}$$

2.1.4.1. Computing the time step. The maximal allowable time step for the numerical scheme obtained on the linearized model is:

$$\Delta t(P_i) = \frac{h(P_i)}{c_i + \|\mathbf{U}_i\|},$$

where $h(P_i)$ is the smallest altitude in the ball of vertex P_i. The global time step is then given by $\Delta t = CFL \min_{P_i}(\Delta t(P_i))$. However, in the context of steady simulation, local time step are used to obtain considerable gain in CPU time. Each vertex advances in time at its own speed defined by its own *CFL* condition.

2.2. Multi-scales anisotropic mesh adaptation

Mesh adaptation provides a way to control the accuracy of the numerical solution by modifying the domain discretization according to size and directional constraints. When dealing with real life flow problems, Hessian-based unstructured mesh adaptation has already proved its efficiency to improve the ratio between the solution accuracy and the number of degrees of freedom (the problem complexity) [6,11,15,23,28,36]. In addition, as a large number of physical phenomena are anisotropic by nature, anisotropic mesh adaptation improves even more this ratio. In the context of flow with shocks, anisotropic mesh adaptation provides very accurate solutions by reducing considerably the numerical dissipation of shock capturing schemes.

If previous features of unstructured mesh adaptation are now quite classical, it has been recently pointed out that mesh adaptation has further consequences impacting directly numerical schemes used to approximate the flow. Indeed, a loss of convergence order generally occurs due to the presence of steep gradients (Naviers Stokes equations) or genuine discontinuities (Euler equations) in the flow, even if a probably spatially high order method is employed. The computed mesh convergence order on uniformly refined meshes is not the theoretical expected one. In [26], it has been demonstrated that the convergence order of numerical schemes can be recovered thanks to this mesh adaptation procedure. Next sections summarize the considered anisotropic mesh adaptation method.

2.2.1. Anisotropic mesh generation

The generation of anisotropic adapted meshes uses the notion of length in a metric space [12]. The idea is to introduce a metric tensor in the dot product definition to modify size evaluation in all directions. In 3D, a metric is a 3×3 symmetric definite positive matrix. The mesh is automatically adapted by generating *a unit mesh* with respect to this metric, *i.e.,* the mesh is such that all edges have a length close to one in the metric and such that all elements are almost regular. The mesh is then uniform in prescribed metric space and, non-uniform and anisotropic in the Euclidean space.

In the context of numerical simulation, the accuracy level of the solution depends on the current mesh used for its computation and the mesh adaptation prescription, *i.e.,* the metric field, is provided by the current solution. This points out the non-linearity of the anisotropic mesh adaptation problem. Therefore, an iterative process needs to be set up in order to converge both the mesh and the solution, or equivalently the metric field and the solution.

2.2.1.1. Mesh adaptation scheme. For stationary simulations, an adaptive computation is carried out *via* a mesh adaptation loop inside which an algorithmic convergence of the pair mesh-solution is sought. In other words, the goal is to converge towards the stationary solution of the problem and similarly towards the corresponding invariant adapted mesh. At each stage, a numerical solution is computed on the current mesh with the flow solver. This solution is analyzed with an error estimate presented in the following section. This error estimate is based on the control of the interpolation error in L^p norm. It provides a metric field. This anisotropic metric is a function of the Hessian of the solution which is reconstructed from the numerical solution. Next, an adapted mesh, *i.e.,* a unit mesh, is generated with respect to this metric. Mesh generators use all the meshing operations to adapt the mesh and a vertex insertion procedure based on an anisotropic generalization of Delaunay technique [10,14]. In this paper, the unstructured adaptive local remesher `Mmg3d` has been used [10]. Finally, the solution is linearly interpolated on the new mesh. This procedure is repeated until convergence of the pair mesh-solution is reached.

2.2.2. Continuous mesh model and optimality

If u denotes a smooth given function, the problem of deriving a mesh that minimizes the L^p norm of the interpolation error is an active field of research [6,8,11,18]. Our approach is based on a promising continuous mesh model that allows to predict effectively the interpolation error on a fictitious so called continuous mesh [25]. In addition to this interpolation estimate, the main benefit is that we are practically able to generate a computational optimal discrete mesh.

Let Ω be a bounded domain of $\mathbb{R}^3$. A continuous mesh $\mathbf{M}$ of domain Ω is a Riemannian metrics space $\mathbf{M} = (\mathcal{M}(\mathbf{x}))_{\mathbf{x}\in\Omega}$ that prescribes at each point $\mathbf{x}$ a density, anisotropic directions and stretching along these directions all given by the metric tensor $\mathcal{M}(\mathbf{x})$. A discrete mesh $\mathcal{H}$ that verifies the anisotropic size prescription of $\mathbf{M}$ is called a unit mesh. It is composed of unit-length edges $\mathbf{e}$ and unit-volume elements K computed in $\mathbf{M}$:

$$\forall \mathbf{e} = \mathbf{pq} \in \mathcal{H}, \quad \|\mathbf{e}\|_{\mathbf{M}} = \int_0^1 \sqrt{{}^t\mathbf{e}\mathcal{M}(\mathbf{p}+t\mathbf{pq})\mathbf{e}}\,dt \approx 1,$$

$$\forall K \in \mathcal{H}, |K|_{\mathbf{M}} = \int_K \sqrt{\det(\mathcal{M}(\mathbf{x}))}\,d\mathbf{x} \approx \frac{\sqrt{2}}{12}.$$

We recall then a first result that follows up from these definitions: if $\mathcal{H}$ is a unit mesh with respect to $\mathbf{M}$ and u is a smooth function, then the following estimate of the linear interpolation error $u - \Pi_{\mathcal{H}}u$ holds:

$$\|u - \Pi_{\mathcal{H}}u\|_{L^p(\Omega_h)} \leqslant \left(\int_\Omega \left(\operatorname{trace}\left(\mathcal{M}^{-\frac{1}{2}}(\mathbf{x})|H_u(\mathbf{x})|\mathcal{M}^{-\frac{1}{2}}(\mathbf{x})\right)\right)^p d\mathbf{x}\right)^{\frac{1}{p}}, \tag{7}$$

where H_u is the hessian of u and $|H_u|$ the matrix deduced from H_u by taking the absolute value of its eigenvalues. The previous inequality turns out to be an equality for some p and some smoothness hypotheses on u. The right-hand side of (7) can be then minimized analytically [2,24], the unique optimal 3D continuous mesh $\mathbf{M}_{L^p} = (\mathcal{M}_{L^p}(\mathbf{x}))_{\mathbf{x}\in\Omega}$ minimizing (7) is:

$$\mathcal{M}_{L^p} = D_{L^p}\,(\det|H_u|)^{\frac{-1}{2p+3}}|H_u| \text{ with } D_{L^p} = N^{\frac{2}{3}}\left(\int_\Omega (\det|H_u|)^{\frac{p}{2p+3}}\right)^{-\frac{2}{3}}, \tag{8}$$

where N is a parameter that fixed the accuracy (size) of the mesh. This parameter is called complexity and is given by:

$$N = \mathcal{C}(\mathbf{M}) = \int_\Omega \sqrt{\det(\mathcal{M}(\mathbf{x}))}\,d\mathbf{x}.$$

D_{L^p} is a global normalization term set to obtain a continuous mesh with a complexity N and $(\det|H_u|)^{\frac{-1}{2p+3}}$ is a local normalization term accounting for the sensitivity of the L^p norm. Indeed, the choice of a L^p norm is essential in a mesh adaptation process regarding the type of problems solved. For instance in CFD, physical phenomena can involve large scale variations. Capturing weak phenomena is crucial for obtaining an accurate solution by taking into account all phenomena interactions in the main flow area. Intrinsically, metrics constructed with lower p norms are more sensitive to weaker variations of the solution whereas the L^∞ norm mainly concentrates on strong singularities (e.g. shocks).

Finally, the interpolation error (7) can be rewritten for $\mathbf{M}_{L^p}$, the following bound follows up for a unit mesh $\mathcal{H}_{L^p}$ with respect to $\mathbf{M}_{L^p}$:

$$\|u - \Pi_{\mathcal{H}_{L^p}} u\|_{L^p(\Omega_h)} \leqslant 3N^{-\frac{2}{3}} \left(\int_\Omega (\det |H_u|)^{\frac{p}{2p+3}} \right)^{\frac{2p+3}{3p}} \leqslant \frac{Cst}{N^{2/3}}. \tag{9}$$

A main result arises from the previous bound: a global second-order asymptotic mesh convergence is expected for the considered variable u. Indeed, a simple analogy with regular grids leads to consider that $N = O(h^{-3})$ so that the previous estimate becomes: $\|u - \Pi_{\mathcal{H}_{L^p}} u\|_{L^p(\Omega_h)} \leqslant Cst' h^2$. The second order convergence property still holds even when singularities are present in the flow field for all $p \in [1, \infty[$, see [26]. This theoretical result is verified numerically in our simulations and is used to assess the obtained numerical solutions

2.2.3. About mesh anisotropy

In three dimensions, mesh anisotropy can be quantified by two notions: the anisotropic ratios and the anisotropic quotients. We first recall both notions and how they are evaluated. Deriving these quantities for an element relies on the fact that there always exists a unique metric tensor for which this element is unit. If $\mathcal{M}_K$ denotes the metric tensor associated with element K, solving the following linear system provides $\mathcal{M}_K$:

$$(S) \quad \begin{cases} \ell^2_{\mathcal{M}_K}(\mathbf{e}_1) = 1 \\ \vdots \\ \ell^2_{\mathcal{M}_K}(\mathbf{e}_6) = 1, \end{cases}$$

where $(\mathbf{e}_i)_{i=1,6}$ is the edges list of K and $\ell^2_{\mathcal{M}_K}(\mathbf{e}_i) = {}^t\mathbf{e}_i \mathcal{M}_K \mathbf{e}_i$. (S) admits a unique solution as soon as the volume of K is not null. Once $\mathcal{M}_K$ is computed, the anisotropic ratio and the anisotropic quotient associated with element K are simply given by

$$\text{ratio} = \sqrt{\frac{\min\limits_i \lambda_i}{\max\limits_i \lambda_i}} = \frac{\max\limits_i h_i}{\min\limits_i h_i}, \quad \text{and} \quad \text{quo} = \frac{\max\limits_i h_i^3}{h_1 h_2 h_3},$$

where $(\lambda_i)_{i=1,3}$ are the eigenvalues of $\mathcal{M}_K$ and $(h_i)_{i=1,3}$ are the corresponding sizes. The anisotropic ratio stands for the maximum elongation of a tetrahedron by comparing two principal directions. The anisotropic quotient represents the overall anisotropic ratio of a tetrahedron taking into account all the possible directions. It corresponds to the overall gain in three dimensions of *an anisotropic adapted mesh* as compared to *an isotropic adapted mesh*. The gain is of course even much greater when compared to a uniform mesh.

2.2.4. Application to numerical computation

In our case, the numerical solution provides a continuous piecewise linear by elements representation of the solution. Consequently, our analysis cannot be applied directly to the numerical solution. The idea is to build a higher order solution approximation u^* of u from u_h which is twice continuously differentiable and to consider u^* in our error estimate. More precisely, the interpolation error is approximated as $\|u - \Pi_h u\|_\Omega \approx \|u^* - \Pi_h u^*\|_\Omega$. If u^* and u_h coincide at mesh vertices then we have $\|u^* - \Pi_h u^*\|_\Omega = \|u^* - u_h\|_\Omega$ illustrating that our estimate approximate the approximation error. Practically, only the Hessian of u^* is recovered. Two recovery (reconstruction) of the Hessian of u^* from u_h, that are compared in this paper, are presented below.

In the context of discontinuous flows, the numerical solution is also piecewise linear by elements even if it approximates a discontinuous solution. The mesh acts as a regularization operator on the solution. In this case, we still approximate the solution u with a continuous higher order representation and we still apply our error estimate. Notice that, even if the numerical solution approximates discontinuous fields, it is continuous due to the numerical dissipation of the numerical scheme.

Let us introduce some notations used in the Hessian recovery methods. Let $\mathcal{H}$ be a mesh of a domain $\Omega_h \subset \mathbb{R}^3$. We denote by $\varphi_i \in V_h$ the basis function associated with vertex P_i, where V_h is the approximation space associated with the P^1 Lagrange finite element. We denote by S_i the stencil φ_i, *i.e.*, $S_i = \operatorname{supp} \varphi_i$, which is in fact the ball of P_i.

2.2.4.1. A double L^2-projection. The local L^2-projection operator is based on the Clément interpolation operator [7]. The idea is to find, in a L^2-norm sense, the best constant gradient on S_i approximating the piecewise constant field by element ∇u_h. For each vertex P_i, we obtain the following gradient reconstruction:

$$\nabla_R u_h(P_i) = \frac{\sum_{K \in S_i} |K| \nabla(u_{h|K})}{|S_i|},$$

where $|K|$ and $|S_i|$ denote the volume of element K and stencil S_i, respectively. In fact, this procedure is equivalent to a reconstruction by means of a volume-weighted averaging.

The recovery procedure provides us with gradient nodal values and thus we get a piecewise linear by elements representation of the gradient. The same recovery procedure is applied to each component of the gradient to recover the Hessian of u^*.

2.2.4.2. A Green formulation. The Hessian of the solution is recovered using a weak formulation, based on the Green formula, considering that the gradient of u_h is constant by element. We consider the same notations as previously. For each vertex P_k of $\mathcal{H}$, we have for $1 \leqslant i,j \leqslant 3$:

$$\int_{\mathcal{H}} \frac{\partial^2 u_h}{\partial x_i \partial x_j}\varphi_k = \int_{S_k} \frac{\partial^2 u_h}{\partial x_i \partial x_j}\varphi_k = -\int_{S_k} \frac{\partial u_h}{\partial x_j}\frac{\partial \varphi_k}{\partial x_i} + \int_{\partial S_k} \frac{\partial u_h}{\partial n}\varphi_k \, d\sigma = -\sum_{K\in S_k}\int_K \frac{\partial u_h}{\partial x_j}\frac{\partial \varphi_k}{\partial x_i},$$

as the shape function is zero on the boundary of the stencil ∂S_k. A specific treatment is done close to the boundary. Each component of the Hessian is then recovered with the relation:

$$\frac{\partial^2 u^*}{\partial x_i \partial x_j}(P_k) := \frac{-\int_{S_k} \frac{\partial u_h}{\partial x_j}\frac{\partial \varphi_k}{\partial x_i}}{\int_{S_k}\varphi_k} = -\frac{\sum_{K\in S_k}\left(\frac{\partial u_h}{\partial x_j}\right)_{|K}\int_K \frac{\partial \varphi_k}{\partial x_i}}{\frac{|S_k|}{4}}.$$

2.3. Adaptive CFD validation by comparison to experimental data

The flow solver `Wolf` coupled with the multi-scales anisotropic mesh adaptation method is validated by comparing on an analytical geometries the numerical results, *i.e.*, mid-field pressure signatures, to experimental data obtained in wind-tunnels by the NASA in experimental studies [5,19]. Two geometries are considered: a simple axisymmetric body and a lifting wing-body. The axisymmetric body is chosen to illustrate the efficiency of the proposed adaptive approach and, to compare and select the resolution parameters. The wing-body configuration validates the methodology on a lifting configuration. The effectiveness in terms of CPU time is also shown.

2.3.1. Axisymmetric body

As in Refs. [21,39], Model 8 of Ref. [5] was selected to validate the proposed approach. This axisymmetric model represents two tandem cones connected by a cylinder defined analytically in inches by:

$$r = x\sqrt{\frac{0.08}{\pi}} \quad \text{if } 0 \leqslant x \leqslant 0.25l$$
$$r = \sqrt{\frac{0.02}{\pi}} \quad \text{if } 0.25l \leqslant x \leqslant 0.75l$$
$$r = \frac{2}{2+\sqrt{2}}\sqrt{\frac{0.04}{\pi}}\left(x - \frac{2-\sqrt{2}}{2}\right) \quad \text{if } 0.75l \leqslant x \leqslant l,$$

with a reference length $l = 2$ inches (5.08 cm). The initial geometry has been elongated by adding a cylinder of length $2l$ to represent the sting support of the wind-tunnel. This geometry is illustrated in Fig. 4. The geometry is immersed in a cylindrical domain aligned with the x-axis. The cylinder has a length of 6 m (236 inches) and a radius of 2.5 m (98 inches). The computation is deliberately fully three-dimensional and do not use any axisymmetric reduction to reduce computational cost. Indeed, the aim is to validate the 3D platform which will be used for complete aircraft configurations that are obviously not axisymmetric. The flow conditions are Mach 1.41 at 0° angle of attack.

While validating the adaptive simulation platform on this test case, the following parameters of the platform are compared:

- HLLC and Roe approximate Riemann solver.
- V4-scheme and V6-scheme.
- L^2-projection and Green Hessian recovery method.

All ran cases are summarized in Table 1.

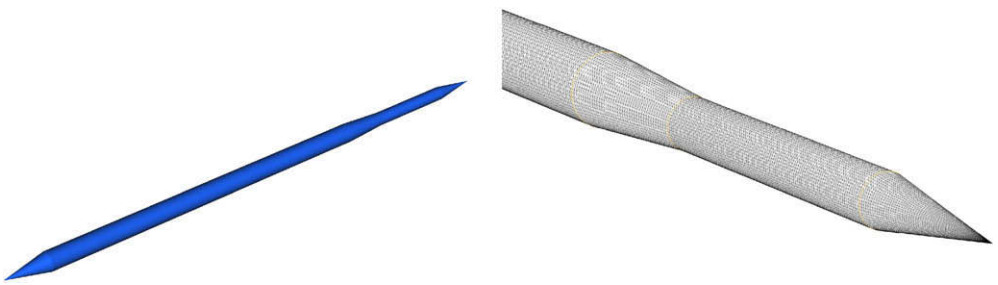

Fig. 4. Axisymmetric spike geometry and surface mesh.

Table 1
All simulations cases for axisymmetric spike geometry. For each case, the final adapted mesh size is given.

Case	Solver	Scheme	Hessian	$\mathcal{H}_{\text{end}}$ # vertices	$\mathcal{H}_{\text{end}}$ # tetrahedra
1	HLLC	V4	L^2-projection	5,107,296	30,315,882
2	Roe	V4	L^2-projection	4,295,057	25,464,860
3	HLLC	V4	Green	4,306,398	25,539,731
4	HLLC	V6	L^2-projection	5,496,361	32,615,241
5	HLLC	V6	Green	4,161,098	24,661,706

The initial uniform mesh is composed of 243,446 vertices and 1,163,402 tetrahedra. As regards mesh adaptation, the Mach number is chosen as sensitive variable and its interpolation error is controlled L^2 norm. A total of 15 adaptation iterations are performed. They are split into 3 steps of 5 adaptations with an increasing complexity:

$$[200,000, 400,000, 800,000].$$

At each step, the couple mesh-solution is algorithmically converged at a fixed complexity. Considering an increasing dynamic complexity level has the advantage to accelerate the convergence of the whole process. In each case, we compared the final solution obtained on the final adapted mesh of almost 5 million vertices and 30 million tetrahedra. To illustrate the kind of mesh obtained, the final mesh obtained for the case 5 is shown in Figs. 5 and 6.

Results are analyzed by extracting the mid-field pressure signatures along lines at various distances under the geometry from 5 to 20 body lengths. More precisely, we plot:

$$\Delta p = \left(\frac{R}{l}\right)^{\frac{3}{4}} \frac{p - p_\infty}{p_\infty} \quad \text{function of } \Delta x = \frac{x}{l}\left(\frac{R}{l}\right)^{-\frac{1}{4}},$$

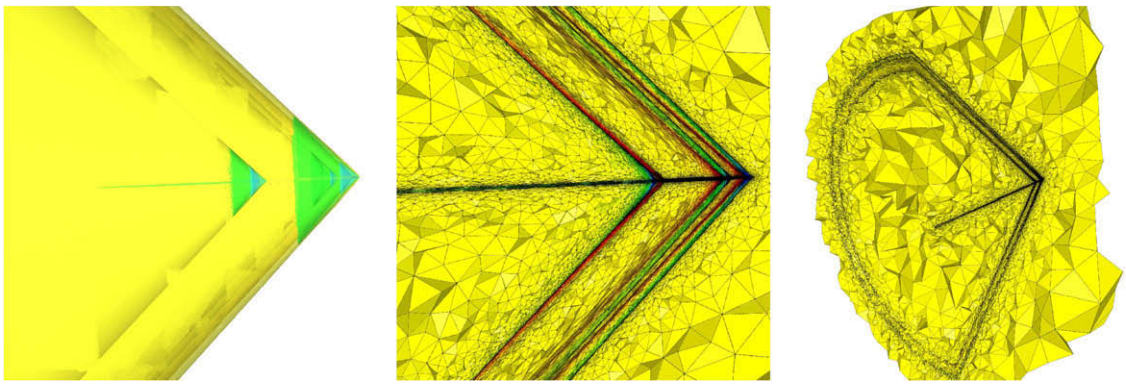

Fig. 5. Axisymmetric geometry. Final adapted mesh and local Mach number solution. Left, the solution iso-surfaces. Middle, adapted mesh and solution iso-values in a plane parallel to the flow. Right, view of the anisotropic adapted mesh.

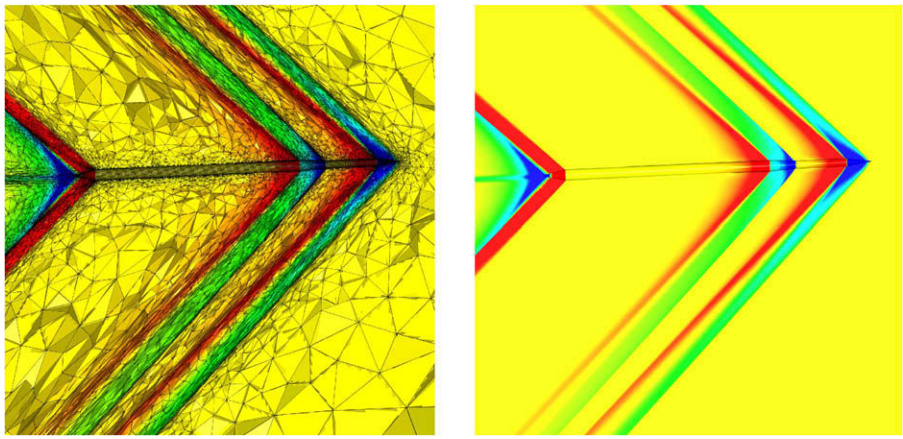

Fig. 6. Axisymmetric geometry. A close view of the final adapted mesh and the solution of case 5.

where R the distance to the body. More details on notations and the extraction procedure are given in Section 3.2. Signatures are compared against NASA experimental wind-tunnel data given in Ref. [5]. For all the cases, the agreement with experimental data is excellent. They are exemplified in Figs. 7–9. Notice that in [5], it is specified that the rounding of the measured pressure peaks is believed to be due in part to wind-tunnel vibration and boundary layer effects. Therefore, sharp shock wave peaks obtained in our simulations are the good answer. Lastly, always in [5], Whitham linear supersonic theory shown good agreement for very simple geometry but discrepancies for the current geometry appear. Whereas the present pressure signatures match the wind-tunnel data. This illustrates the benefits of the proposed approach which will be even more crucial when dealing with complex aircraft geometries. The discussion on Whitham theory will be pursued in Section 3.2.

To compare the numerical results, two points conduct our analysis on the mid-field signatures:

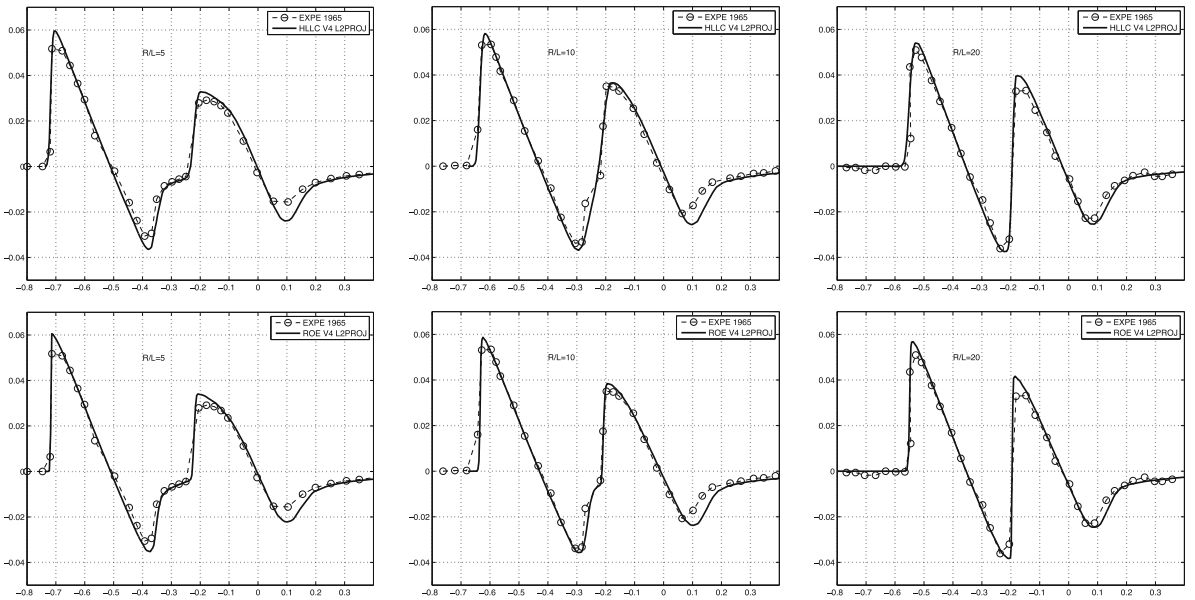

Fig. 7. Axisymmetric geometry. Comparison between HLLC (top) and Roe (bottom) Riemann solvers. In both cases, the V4-scheme and a double L^2-projection for the Hessian reconstruction have been used.

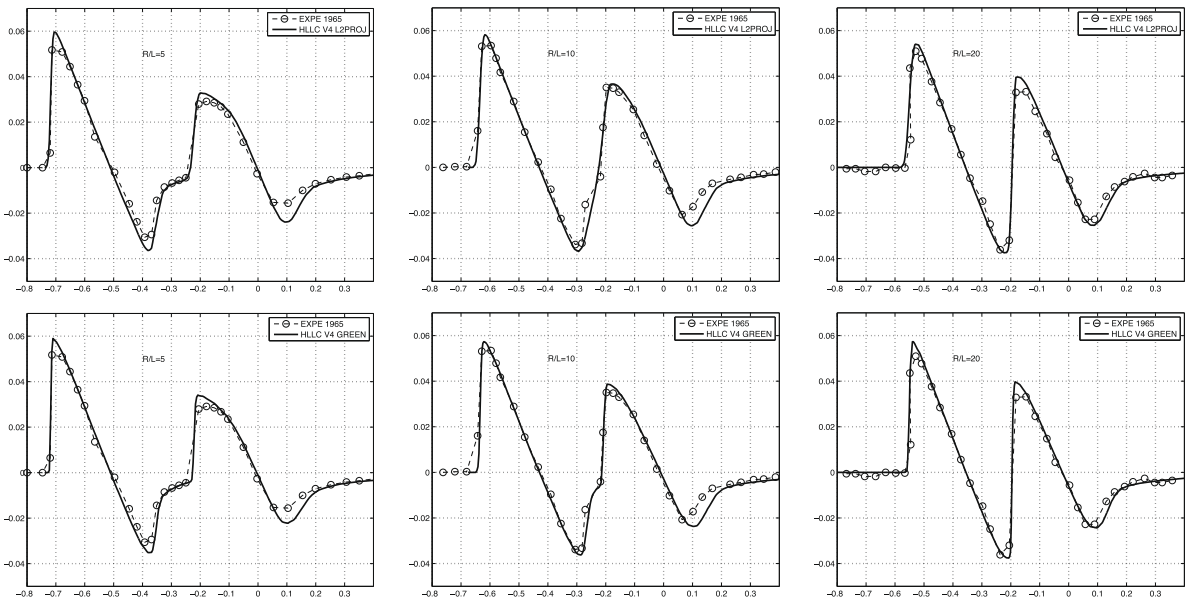

Fig. 8. Axisymmetric geometry. Comparison between the double L^2-projection (top) and the Green formula (bottom) for the Hessian reconstruction. In both cases, the V4-scheme with the HLLC Riemann solver have been used.

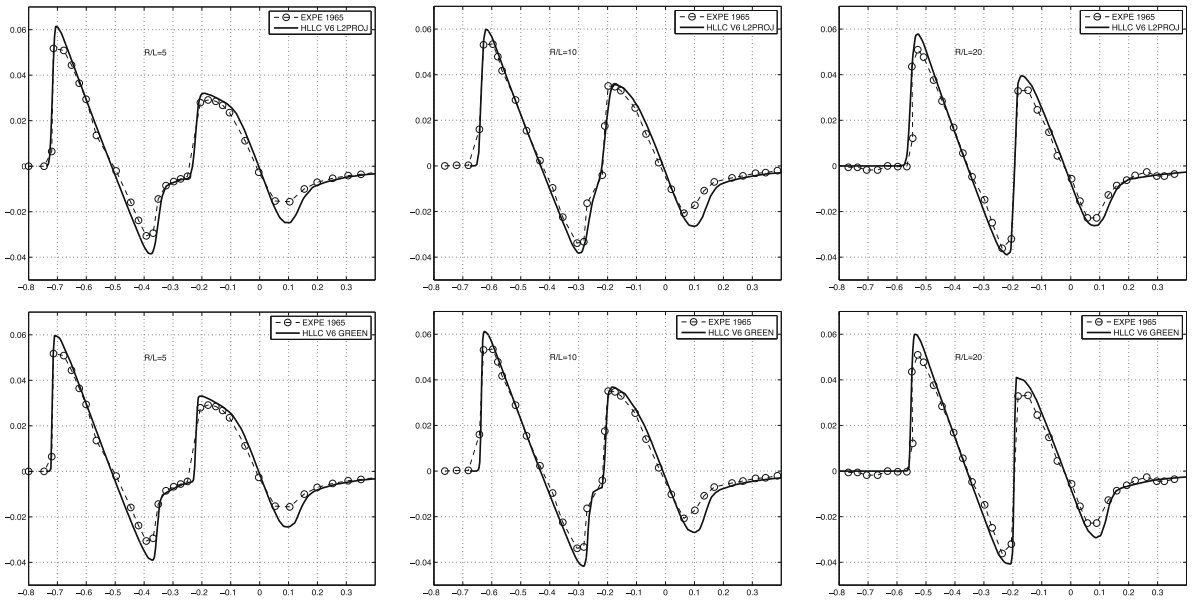

Fig. 9. Axisymmetric geometry. Comparison between the double L^2-projection (top) and the Green formula (bottom) for the Hessian reconstruction. In both cases, the V6-scheme with the HLLC Riemann solver have been used.

1. The sharpness and the intensity of the shock waves at $R/l = 20$. In Section 3.2, we will see that the pressure decrease law in the mid-field is proportional to $(R/l)^{\frac{3}{4}}$ and the time length of the wave grows in $(R/l)^{\frac{1}{4}}$. And asymptotically, the pressure decrease law is in $(R/l)^{\frac{1}{2}}$. Therefore, the shocks amplitude must preserved (or increased) through the propagation, else it points out a numerical dissipation of the flow solve.
2. The last two shocks that are located between $\Delta x = 0.2$ and $\Delta x = 0.4$ at $R/l = 5$ are still separated at $R/l = 10$. This means that the two last shocks focalize at a distance between $R/l = 10$ and $R/l = 20$. If the two shocks have focalized before $R/l = 10$, it is an artifact due to the numerical dissipation of the flow solver.

In all cases, the Dervieux limiter is specified and the 5-stage order-2 SSPRK scheme is used for the time integration.

2.3.1.1. Roe vs. HLLC. The comparison between the Roe and the HLLC Riemann solvers is presented in Fig. 7. For the analysis, both schemes are coupled with the V4-scheme and the L^2-projection Hessian recovery which correspond to cases 1 and 2. As expected, Roe is more accurate than HLLC. The difference in accuracy between each case is highlighted on the last two shocks that are not still merged at $R/l = 10$ for Roe. Moreover, the numerical dissipation of the solver is identified by the loss of intensity of the first shock peak which must remain constant. This phenomena is weaker with the Roe Riemann solver. However, for robustness purposes, we prefer the HLLC Riemann solver as on more complex geometries with complex boundary conditions, such as real aircraft with engine presented in Section 4, the Roe Riemann solver can lead to negative pressures.

2.3.1.2. L^2-projection vs. Green. The Hessian recovery methods are compared by using the HLLC Riemann solver and by considering either the V4-scheme (cases 1 and 3) shown in Fig. 8 or the V6-scheme (cases 4 and 5) presented in Fig. 9. The Green reconstruction is clearly the best choice than the L^2-projection for this application. Indeed, in cases 1 and 4 the separation between the two last shocks disappeared at $R/l = 10$ whereas this separation is still present in cases 3 and 5 with the Green reconstruction in spite of the fact that adapted meshes with the Green reconstruction contain one million less vertices. This difference in accuracy is essentially due to the smallest (minimal) stencil of the Green recovery procedure. It results that the information to compute the metric is more compact (a three-vertices stencil) with the Green formulation than with the L^2-projection reconstruction (a five-vertices stencil). Therefore, larger second derivatives are computed in the direction normal to shock waves implying smallest sizes to be prescribed by the metric along shock waves.

2.3.1.3. V4-scheme vs. V6-scheme. The V6-scheme improves pressure signatures whatever the considered Riemann solver or the considered Hessian construction. This impact is highlighted when comparing Figs. 8 and 9. Even if this scheme was initially designed to capture more accurately smooth solutions, such as vortices or instabilities, it also computes sharper shocks and reduces the numerical dissipation when propagating shocks.

2.3.1.4. Conclusion. The combination HLLC Riemann solver, V6-scheme and Green formulation for the Hessian recovery provides very accurate results agreeing with the experimental data, cf. Fig. 9 right. The shock waves are not dissipated during

the propagation and the shock sharpness is preserved. It demonstrates the ability of unstructured CFD flow solvers coupled with mesh adaptation to provide accurate results in the mid-field, here $R/l = 20$.

2.3.2. Lifting wing-body

The aim of this section is to validate the adaptive CFD model on a lifting configuration proposed by NASA and to point out that the method can accurately predict full 3D configurations. A lifting wing-body produces a flow field disturbance which is proportional to the degree of lift generated. The typical run time of the adaptive loop is also given.

Model 4 geometry of wind tunnel study [19] is selected. This configuration has also been studied in [39]. This lifting wing-body geometry consists of an axisymmetric fuselage and a sweep delta wing. The body is a cylinder with a parabolic nose of length 17.52 cm and diameter 1.08 cm. The fitness ratio (l/d) is thus 16.22. The thickness r of the parabolic nose, of length 7.01, is defined by

$$r = 0.54 - 0.011(x - 7.01)^2.$$

The wing is a 69° leading edge sweep delta wing and double-wedge 5-percent-thick diamond sections with the ridge line located at mid-chord. The wings are mounted on the cylindrical portion of the fuselage at the longitudinal plane of symmetry at $x = 8.21$ cm. The dimensions of the wing tunnel sting are not provided in [19]. Based on this limited data, the sting is represented by a simple body of revolution extending 4 body-lengths behind the aircraft. The sting geometry is exactly the same as the one in Ref. [39]. The geometry is immersed in a cylindrical domain aligned with the x-axis. The cylinder has a length of 2.75 m and a radius of 80 cm. This geometry is illustrated in Fig. 10.

The flow conditions are Mach 1.68 and a lift coefficient (C_L) of 0.08. The angle of attack was set to match the desired lift using the reference area equal to 33.106 cm^2.

Based on the previous analysis, for the flow solver, we have specified the HLLC Riemann solver, the V6-scheme with the Dervieux limiter and for the temporal integration the 5-stage order-2 SSPRK scheme.

The multi-scales mesh adaptation considers a control of the interpolation error in L^2 norm of the local Mach number. A mesh gradation of 2 has been set with an increase law coefficient of 1.1 [1]. A total of 10 adaptations have been performed split into 2 steps of 5 adaptations. At each step, the pair mesh-solution is algorithmically converged at a fixed complexity. We have fixed a complexity of 15,000 for the first step and 30,000 for the second one. It results in a final adapted mesh the size of which is almost 430,000 vertices.

The final mesh and its associated solution, the C_p iso-values, are shown in Fig. 11. The flow field is accurately computed in the whole domain in the sense that the solution has not been diffused throughout its propagation in the mid-field. In particular, the shock waves have been propagated up to the domain boundaries. This result points out that the numerical dissipation of the flow solver has been drastically reduced thanks to the anisotropic mesh refinement.

The accuracy of the obtained solution is deeper analyzed by a comparison to the experimental data of [19]. The mid-field pressure signature is extracted at 3.6 body lengths, $R/L = 3.6$, under the geometry at the end of each step of the adaptation loop. More details on the extraction procedure are given in Section 3.2. The pressure signal plot, Fig. 12 middle-left, shows very good agreement with the wind tunnel data. As in [39], we observe a discrepancy between the numerical solution and the experiment for $x \in [1; 1.1]$ probably due to the inaccurate representation of the body sting.

This accurate solution, in the whole domain, has been obtained on a relatively coarse mesh "only" composed of 430,000 vertices. This complexity reduction is achieved by the mesh anisotropy. The mesh anisotropy is quantified by the anisotropic ratios and the anisotropic quotients, as explained in Section 2.2.3. The mean anisotropic ratio is 34 and the mean anisotropic quotients is 722. The last quantity signifies that the anisotropy leads to a mesh complexity reduction of almost three order of magnitudes as compared to an isotropic adapted mesh. Detailed histograms of the anisotropic ratio and quotient are given in Table 2.

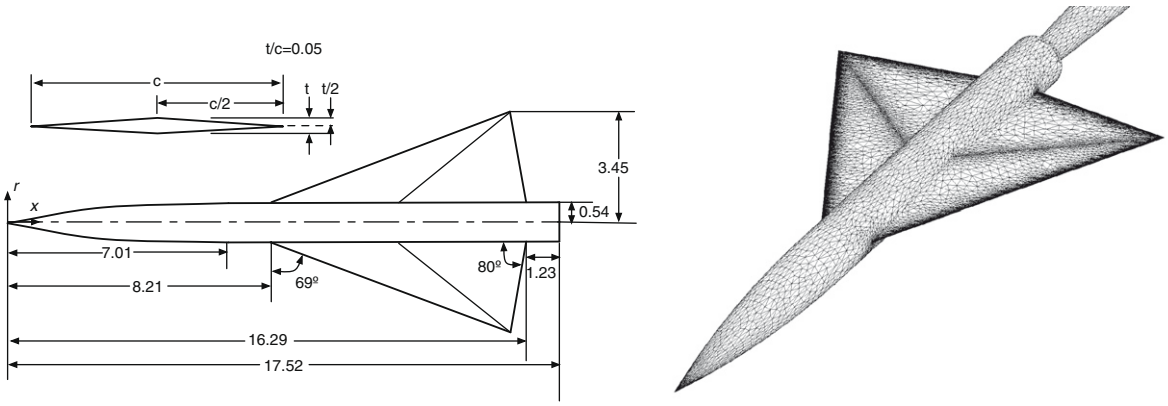

Fig. 10. Left, model 4 lifting wing-body geometry of [19]. Right, lifting wing-body surface mesh.

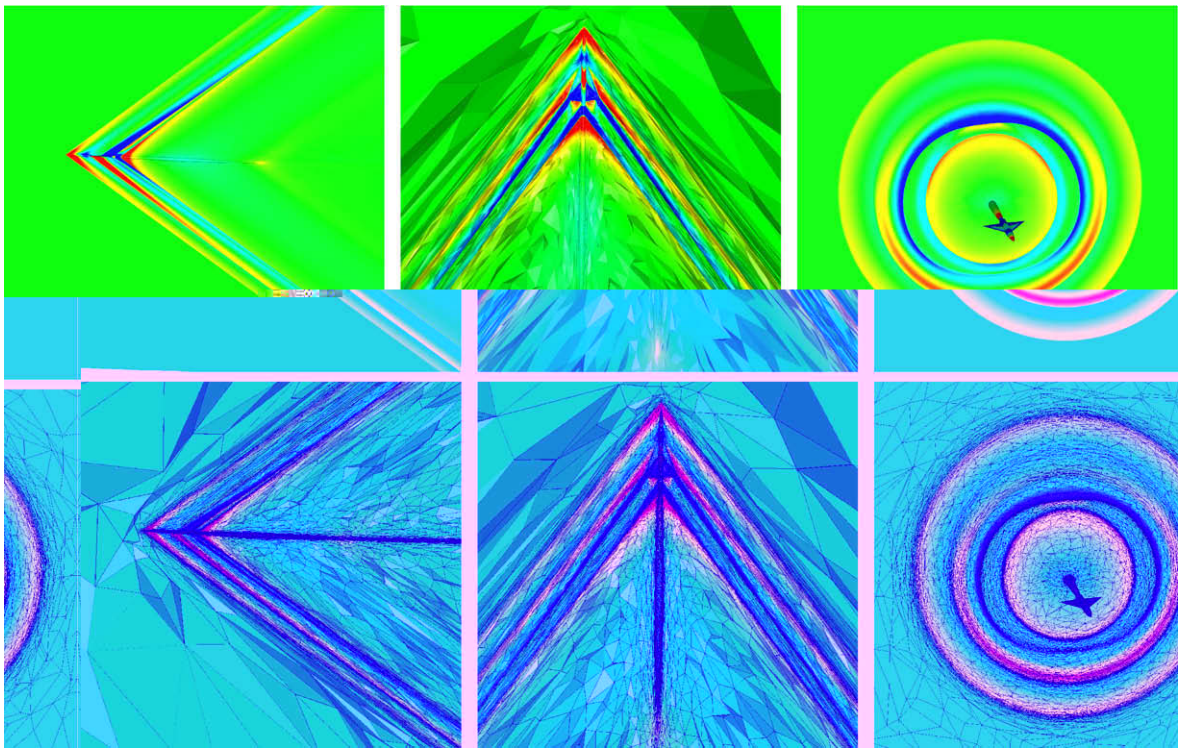

Fig. 11. Lifting wing-body. C_p iso-values (top) and final adapted mesh (bottom) for three cut planes. Left, the symmetry plane $y = 0$, middle, the plane $z = 0$ and, right, the plane $x = 0.35$.

This simulation is run on a eight-processors 64-bits Mac Pro with an Intel Core 2 chipsets with a clock speed of 2.8 GHz with 16 Gb of RAM. The CPU time for the whole computation is 2 h. The flow solver consumes 85% of the CPU time. Detailed wall-clock time for each step of the adaptation loop are reported in Table 3. Note that 20 min of CPU times have to be added to the flow solver to compute the initial state on the initial mesh.

2.3.2.1. Additional validation. The two additional lift conditions for Mach 1.68 presented in [19] are considered. Exactly the same data are set for each simulation. The pressure signals predicted for $C_L = 0$ and $C_L = 0.15$ at each step of the adaptation loop are shown in Fig. 12 left. In both cases, agreement with the wind tunnel data is very good. The CFD solutions are obtained with relatively coarse meshes.

Finally, the three additional cases at higher Mach, $M = 2.7$, for C_L equal to 0, 0.08 and 0.15 of [19] are run. For these cases, a simple cylindrical sting has been added to the geometry instead of the original one. The comparison to the wind tunnel data is done by observing the pressure signal at $R/L = 3.1$. Again, agreement with the experimental data is good, see Fig. 12 right, except for the last shock corresponding to the region associated with the juncture between the body and the sting. A more accurate representation of the sting would probably improved the results.

2.4. CFD validation without experimentation

When no experimental data are available, the computations can be validated by checking the convergence order of the method. In our case, the second order predicted by the theory has to be asymptotically attained on a series of (almost) embedded meshes. This will be done in Section 4 to validate the aircraft simulations. Another possible approach is to match in the mid-field the CFD pressure signal with a signal propagated from the near-field.

3. Sonic boom modeling

Due to the complexity of the phenomenon, an accurate simulation of sonic boom signals at the ground requires to couple non-linear CFD models and linear acoustic propagation equations. The near-field and mid-field flows are computed by solving the Euler equations with the adaptive techniques presented previously. The pressure distribution obtained under the aircraft in the mid-field region is used to set up the initial conditions for the propagation of the acoustic waves to the ground. This propagation is achieved with a one-dimensional simplified model resulting in the sonic boom signature. However, the

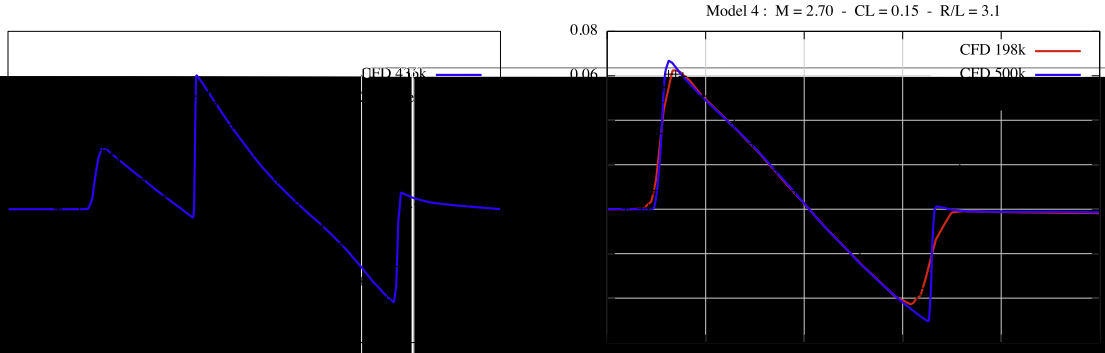
Model 4 : M = 2.70 - CL = 0.15 - R/L = 3.1
0.08
0.06
CFD 198k
CFD 500k

Table 2
Anisotropic ratio (left) and quotient (right) histograms for the lifting wing-body final adapted mesh composed of 2,195,005 tetrahedra. For each interval, the number of tetrahedra is given with the corresponding percentage.

	Lifting wing-body	(%)
Anisotropic ratio		
$1 < \text{ratio} \leqslant 2$	10,336	0.47
$2 < \text{ratio} \leqslant 3$	53,258	2.43
$3 < \text{ratio} \leqslant 4$	82,892	3.78
$4 < \text{ratio} \leqslant 5$	93,021	4.24
$5 < \text{ratio} \leqslant 10$	370,925	16.90
$10 < \text{ratio} \leqslant 50$	1,098,248	50.03
$50 < \text{ratio} \leqslant 100$	371,695	16.93
$100 < \text{ratio} \leqslant 1000$	114,255	5.21
$10^3 < \text{ratio} \leqslant 10^4$	375	0.02
Mean ratio	34	
Mean quotient	722	
Anisotropic quotient		
$1 < \text{quo} \leqslant 2$	2312	0.11
$2 < \text{quo} \leqslant 3$	14,254	0.65
$3 < \text{quo} \leqslant 4$	24,578	1.12
$4 < \text{quo} \leqslant 5$	29,310	1.34
$5 < \text{quo} \leqslant 10$	148,446	6.76
$10 < \text{quo} \leqslant 50$	476,068	21.69
$50 < \text{quo} \leqslant 100$	213,790	9.74
$100 < \text{quo} \leqslant 1000$	938,658	42.76
$10^3 < \text{quo} \leqslant 10^4$	337,882	15.39
$10^4 < \text{quo} \leqslant 10^5$	9256	0.42
$10^5 < \text{quo} \leqslant 10^6$	406	0.02
$10^6 < \text{quo}$	45	0.00

Table 3
CPU times for each step of the mesh adaptation loop for the lifting wing-body test case at $M = 1.68$ and $C_L = 0.08$.

Step	Solver	Metric	Mesh	Interpolation	Global
Total CPU time	1 h 40 m 33 s	1 m 04 s	16 m 31 s	37 s	1 h 58 m 45 s
Percentage (%)	84.68	0.90	13.90	0.52	100

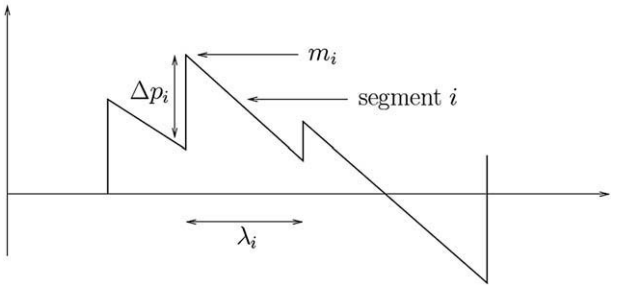

Fig. 13. Illustration of the three parameters $m_i, \Delta p_i$ and λ_i characterizing the pressure wave.

A system of three ordinary differential equations (ODEs), one for each parameter, is solved to propagate the pressure wave in atmosphere:

$$\begin{cases} \frac{dm_i}{dt} = C_1 m_i^2 + C_2 m_i, \\ \frac{d\Delta p_i}{dt} = \frac{1}{2} C_1 \Delta p_i (m_i + m_{i-1}) + C_2 \Delta p_i, \\ \frac{d\lambda_i}{dt} = -\frac{1}{2} C_1 (\Delta p_i + \Delta p_{i+1}) - C_1 m_i \lambda_i, \end{cases} \tag{10}$$

with notations:

$$C_1 = \frac{\gamma + 1}{2\gamma} \frac{c}{p a_n} \quad \text{and} \quad C_2 = \frac{1}{2} \left(\frac{3}{c} \frac{dc}{dt} + \frac{1}{\rho} \frac{d\rho}{dt} - \frac{2}{a_n} \frac{da_n}{dt} - \frac{1}{A} \frac{dA}{dt} \right),$$

where c, ρ and p are the air ambient sound speed, the density and the pressure, respectively. We have denoted by a_n the speed at which a wave propagates along the acoustic ray cone and A the acoustic ray tube area as cut by the waveform (*i.e.*, the Mach cone), cf. Fig. 14. All these quantities are functions of the altitude. The speed at which a wave propagates along the acoustic ray cone is given by $a_n = c + \mathbf{v}.\mathbf{n}$ where $\mathbf{v}$ is the wind velocity and $\mathbf{n}$ the wavefront unit normal. If the wind velocity is assumed to be zero then we have $a_n = c$.

Acoustic rays are emitted by the aircraft and propagate orthogonally to the wavefronts. They represent the paths (*i.e.*, the geodesics) along which the acoustic disturbance propagates in atmosphere. They form the *ray tube* or *ray cone*, cf. Fig. 14. The initial direction of a ray is given by the ray cone near the aircraft which is orthogonal to the Mach cone. To compute the ray tube area, four rays are selected, separated by a time increment and an azimuthal increment. The initial directions of these rays are governed by the aircraft flight parameters and the considered azimuth. With these initial conditions, ray paths can be traced. Rays are traced by direct numerical integration of the eiconal. All four rays are traced in this way and the ray tube area is computed by numerical differencing. Detailed formulae to compute wavefront unit normal and ray tube area are given in [16]. In this study, we only analyze sonic boom signature for an angle of emission (or azimuthal angle) of acoustical rays equal to zero.

Atmosphere has to be defined to evaluate these quantities, *i.e.*, the temperature and the pressure evolution have to be specified as a function of the altitude. Here, we consider the ICAO Standard atmosphere [20]. This atmosphere is accurately represented by the following analytical functions:

$$T(z) = \max(T_{gnd} - 6.5z, 216.65),$$
$$p(z) = \begin{cases} p_{gnd}\left(1 - \frac{6.50\,z}{T_{gnd}}\right)^{5.26} & \text{if } 0 \text{ km} < z < 12.25 \text{ km}, \\ p_{gnd}\left(1 - \frac{3.04\,z}{T_{gnd}}\right)^{12.26} & \text{if } 12.25 \text{ km} < z < 30 \text{ km}, \end{cases}$$

where $T_{gnd} = 288.15$ K and p_{gnd} = 101,300 Pa are the temperature in Kelvin and pressure in Pascal at the ground, respectively. Moreover, we assume that the air is following the perfect gas rule. A complementary hypothesis is made by assuming that there is no-wind between the flight altitude and the ground.

To solve this system, the three ordinary differential equations of System (10) are integrated in time by considering sufficiently small time steps in order to be able to assume that variables C_1 and C_2 are constants. Moreover, the time steps must be adequately truncated throughout the resolution. Indeed, as the wave propagates down the ray path, shocks will coalesce to form a new one. When this occurs one or more of the λ_i will go to zero. When one of the λ_i does go to zero somewhere between two points on the ray path, the associated segment is suppressed and the waveform parameters must be redefined. The ground reflexion is taken into account by a reflexion coefficient equal to 1, thus implying pressure doubling at the ground surface (altitude 0) because of the reflexion.

3.2. Coupling CFD and wave propagation

The acoustic propagation code uses the mid-field solution of the Euler code as initialization. More precisely, a pressure distribution is extracted under the aircraft in the mid-field region to set up initial conditions for the propagation. The extraction is presented in the next paragraph. To ensure a valid coupling, the solution where the initial signal is extracted must verify the Whitham linear supersonic aerodynamic theory. Those conditions are explained in the last paragraph.

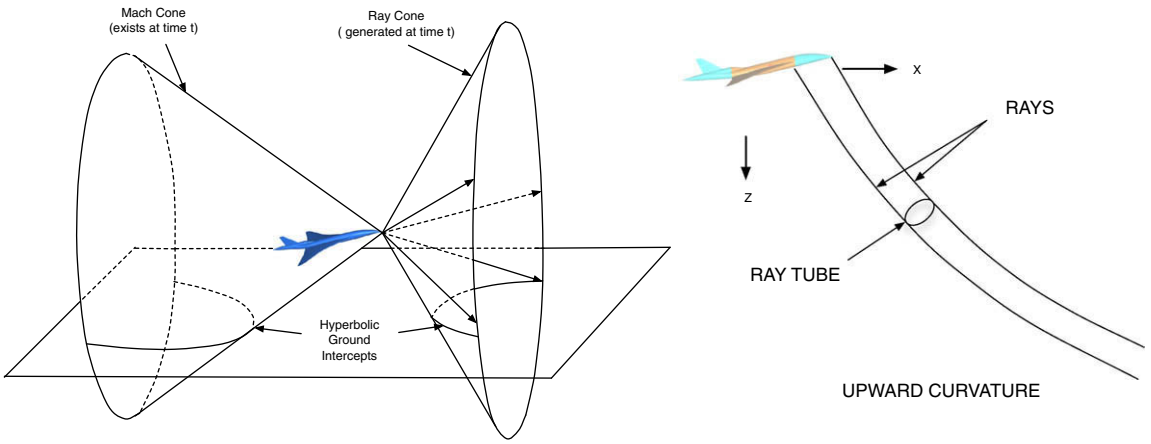

Fig. 14. Left, definition of the ray cone which represents the paths along which the acoustic disturbance propagates. Right, definition of ray tube and its area.

Let us first introduce the used nomenclature. We denote by:

- α the angle of attack of the aircraft
- M the Mach number
- p the acoustical pressure and p_∞ the atmospherical pressure
- β is the Mach cone angle with the flow direction defined by $\sin\beta = \frac{1}{M}$
- L is the length of the aircraft
- R the distance of the observation point from the line parallel to the flow direction (or the ground) going through the nose of the aircraft
- θ is the azimuthal angle or the emission angle.

In practice, the distance from the aircraft is expressed with the ratio R/L.

3.2.1. Source signature extraction

Assuming that the aircraft is flying along the x-axis from positive to negative x, the extraction line at distance 0, or $R/L = 0$, is the line going through the nose of the aircraft with an angle of α in the symmetric plane Oxz. In other words, a line parallel to the flow direction going through the nose of the aircraft. This line is defined by its two extrema:

$$\begin{cases} x_0 = x_{\text{jet}} - l_{\text{front}}\cos\alpha \\ y_0 = y_{\text{jet}} \\ z_0 = z_{\text{jet}} - l_{\text{front}}\sin\alpha \end{cases} \quad \text{and} \quad \begin{cases} x_1 = x_{\text{jet}} + (L + l_{\text{back}})\cos\alpha \\ y_1 = y_{\text{jet}} \\ z_1 = z_{\text{jet}} + (L + l_{\text{back}})\sin\alpha \end{cases}$$

where $P_{\text{jet}} = (x_{\text{jet}}, y_{\text{jet}}, z_{\text{jet}})$ is the nose of the aircraft and, l_{front} and l_{back} are the length of the line before the nose and after the tail of the aircraft, respectively. The extraction line at a given distance R/L is obtained by translating it along the Mach cone:

$$\begin{cases} x_i^{R/L} = x_i + R\frac{\cos(\beta-\alpha)}{\sin\beta} \\ y_i^{R/L} = y_i \\ z_i^{R/L} = z_i - R\,\frac{\sin(\beta-\alpha)}{\sin\beta} \end{cases} \quad \text{for } i = 0, 1.$$

Finally, the extraction line at a given R/L and a given azimuthal angle θ is defined by:

$$\begin{cases} x_i^{R/L,\theta} = x_i + R\cos\theta\sin\alpha + R\frac{\cos\alpha}{\tan\beta} \\ y_i^{R/L,\theta} = y_i + R\sin\theta \\ z_i^{R/L,\theta} = z_i - R\cos\theta\cos\alpha + R\frac{\sin\alpha}{\tan\beta} \end{cases} \quad \text{for } i = 0, 1.$$

In all this study, we only consider extraction line at azimuthal angle 0.

The pressure variation along the extraction line is used as an initial input for the propagation code. In our implementation, this line corresponds to a uniform *a posteriori* discretization along the flight path. The pressure values on this discretization are obtained by interpolating linearly the aerodynamic near-field pressure. To this end, each point of the line is localized in the tetrahedral CFD mesh, *i.e.,* we find the tetrahedron to which it belongs. In our approach, the segment discretization is finer than the one used in the CFD computation. Practically, the initial input for the propagation code is the pressure variation:

$$\delta p = \frac{p - p_\infty}{p_\infty}.$$

3.2.2. Validity of the coupling

The flow near the aircraft is three-dimensional and non-linear in nature whereas the propagation is a linear one-dimensional model. The coupling between these two models becomes valid if the mid-field pressure signal can be used, as a F-function, to initialize the propagation. As stated in [30], there is a matching radius between the source function and the propagation extrapolation. The assumption, that has not been rigorously verified, is that the use of the pressure signal become valid when the flow field does not contain crossflow components anymore. In other words, the flow field is locally axisymmetric and it has no more non-linear effect. As crossflow components are very significant at small radii but are less at larger distances, the pressure signal has to be extracted in the mid-field far enough from the aircraft to respect such a condition. This is a necessary condition to take all the elements of the aircraft geometry (body, wings, ...) into account in the sonic boom signature.

This condition can be verified according to the linear supersonic aerodynamic theory. Experimentally (see for instance the results of Section 2.3), the law variation of the pressure front δp decreases proportionally to $R^{-\frac{3}{4}}$ (equivalently $(R/L)^{-\frac{3}{4}}$) while the duration of the wave grows in $R^{\frac{1}{4}}$ (see also Section 2.3). The pressure decrease law tends toward R^{-1} near the mobile where high non-linearities occur. And, this law tends toward $R^{-\frac{1}{2}}$ when the non-linear effect become negligible. To summarize, the CFD flow field is considered converged and locally axisymmetric if the pressure variation tends to decrease proportionally to $(R/L)^{-\frac{1}{2}}$. Nevertheless, such a condition has to be verified carefully. Indeed, a non-linearity diffusing behavior may

appear in the solution due to the numerical dissipation of the flow solver. In particular, if the CFD mesh is not refined enough, shock waves will be diffused throughout their propagation and non-linearities will be removed.

As a consequence, multi-scales anisotropic mesh adaptation can remedy this issue as it controls globally the mesh sizes and guarantees a coherent numerical dissipation in the whole computational domain. In order to certify the propagation, we analyze the convergence of the sonic boom signature with respect to the extraction distance.

4. Studying the sonic boom of several SSBJs

In this section, we study and compare three supersonic business jet (SSBJ) geometries that have been provided by Dassault Aviation during the HISAC european project [17].

The first aircraft, cf. Fig. 17 top, is a low-drag-shaped jet. In the following, we will refer to as the **low drag** jet. This geometry is the simplest one. In particular, the engines have not been integrated while it is known that they have a significant impact on the sonic boom. The length of this jet is $L = 37$ m and it has a wing span of 17 m. The surface mesh accuracy varies between 1 mm and 30 cm.

The second aircraft is a low-boom-shaped jet. This geometry is more complex than the previous one. Notably, the engine have been integrated. We notice that the engine have been integrated over the fuselage to minimize the impact of the

Table 4
Number of vertices and of tetrahedra for the final adapted meshes.

Geometry	$\mathcal{H}_{\text{final}}$ # vertices	$\mathcal{H}_{\text{final}}$ # tetrahedra
Low drag	9,465,835	56,568,966
Low boom	9,077,197	53,842,961
Low boom + dihedral	9,083,531	53,884,863

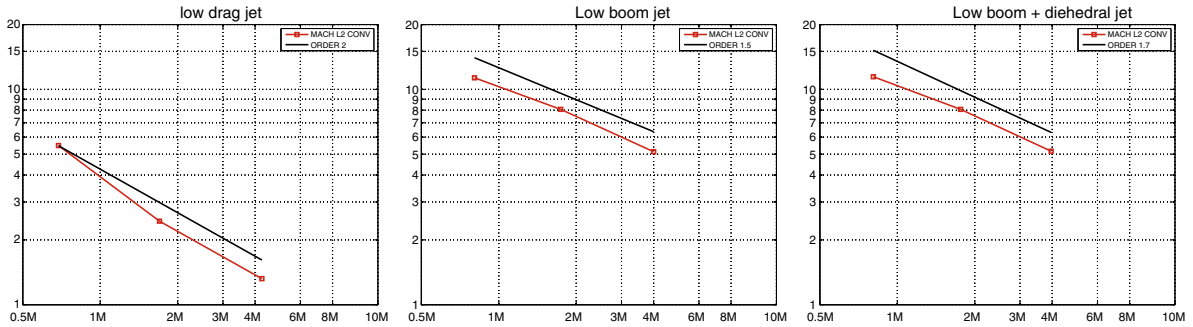

Fig. 15. Global mesh convergence order for each SSBJ. From left to right, we obtain an order of 2 for the low drag jet, 1.5 for the low boom jet and 1.7 for the low boom + dihedral jet.

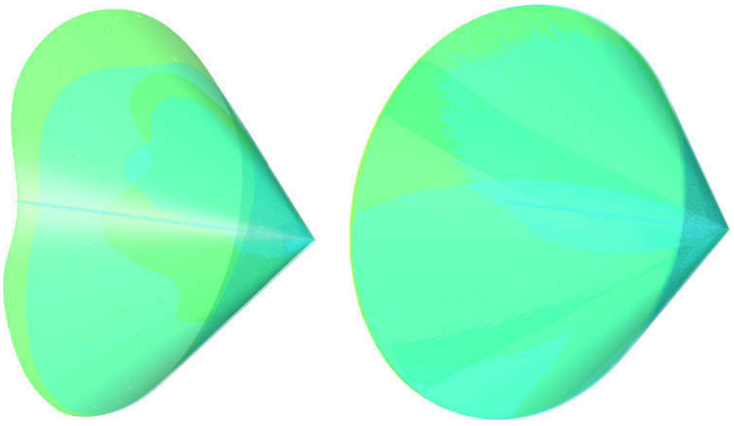

Fig. 16. Left, the Mach cone emitted by the low boom + dihedral SSBJ. Right, the Mach cone emitted by the low drag SSBJ. The maximal Mach cone diameter is 1.25 km.

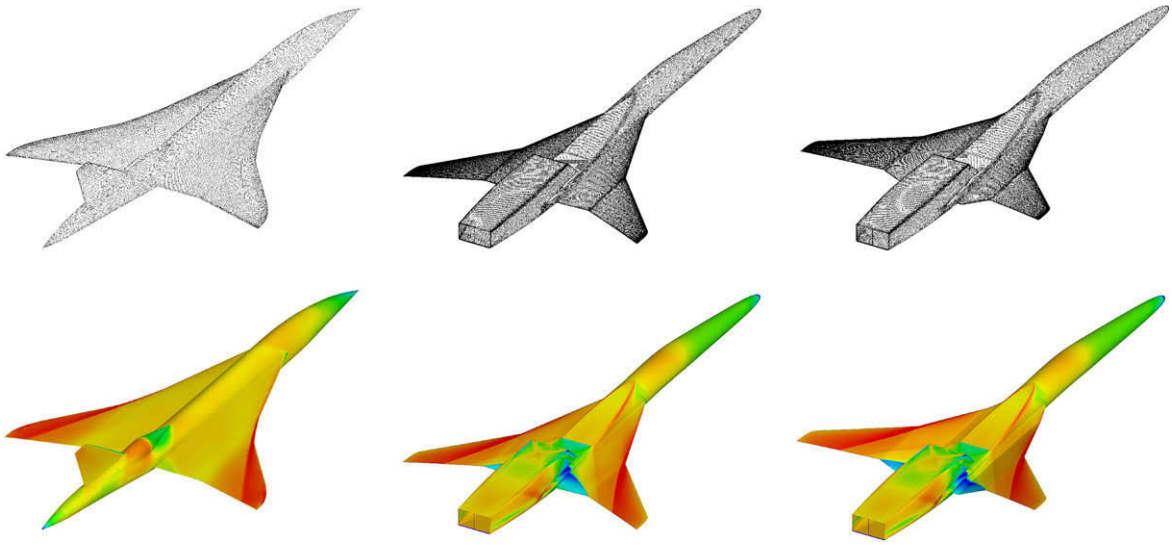

Fig. 17. From top to bottom, the three studied configurations: the low drag jet, the low boom jet and the low boom + dihedral jet. Left, the surface meshes, and right, the local Mach number iso-values.

nacelles on the sonic boom. The aircraft length is $L = 42$ m and it has a wing span of 20 m. The surface mesh accuracy varies between 0.2 mm and 12 cm. This represents already a size variation of five orders of magnitude with respect to the aircraft size, and this only for the surface mesh. Two versions of this jet are studied. The difference between them is the wing. The first one has flat wing, it is represented in Fig. 17 (middle). We name it **low boom** jet. For the second

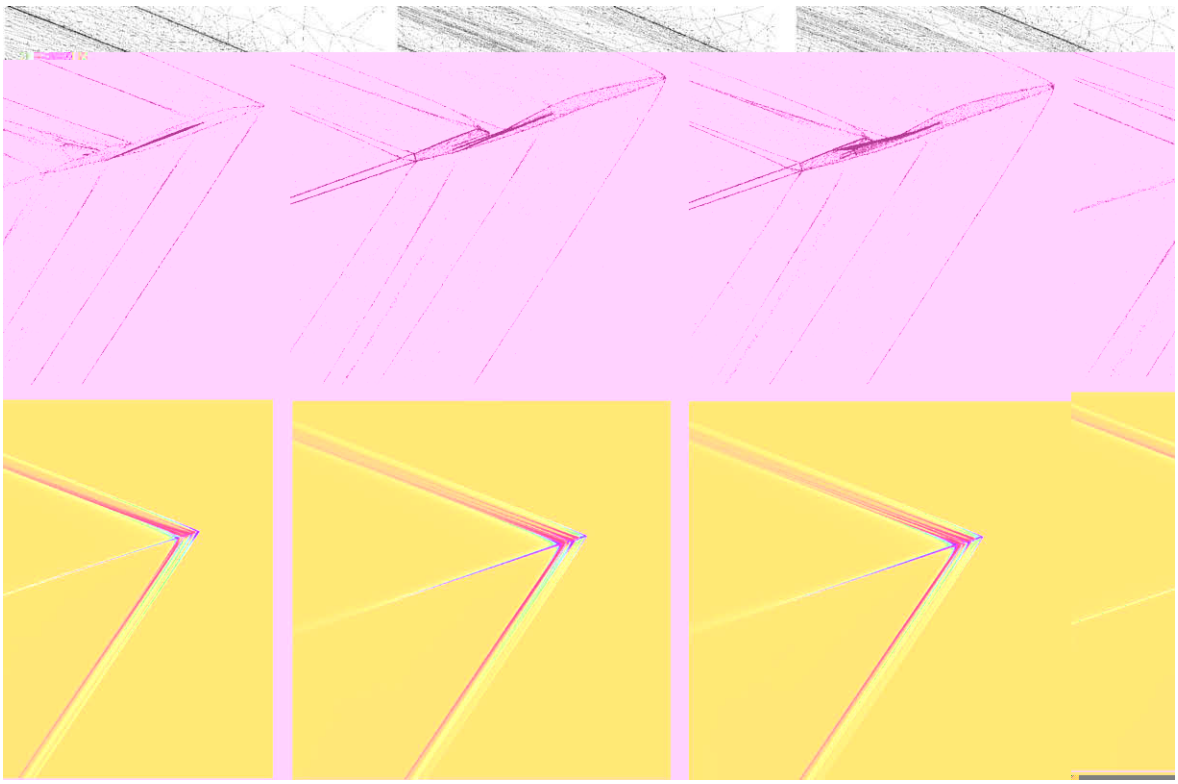

Fig. 18. From top to bottom, the low drag jet, the low boom jet and the low boom + dihedral jet. Left, view of the adapted volume mesh through the cut plane along 0*xz*, and right, the associated local Mach number iso-values.

shape, the wing has a double dihedral angle, Fig. 17 (bottom). The first dihedral angle is at the junction of the wing and the fuselage. The second one is where the wing swept angle change. The wing differences are clearly visible in Fig. 21. This second shape will be refer as the **low boom + dihedral** jet. With this geometry, wing dihedral angles effectiveness on the sonic boom will be analyzed.

The computational domain is a cylinder of 2.25 km length and 1.5 km diameter. This represents a scale factor of 10^7 if the size of the domain is compared to the maximal accuracy of the low boom jet surface mesh. This domain size enables pressure signature in the mid-field to be obtained up to $R/L = 19$ for the low drag jet and $R/L = 16$ for both low boom models. The aim here is to perform large R/L computations together with a convergence study to assess the numerical results.

This results section is outlined as follow. First, the parameters of the study are given. Then, the global orders of convergence of each simulation are presented and the CFD results obtained for the near-field and mid-field are discussed. The achieved mesh anisotropy is examined for each computation. In a fifth subsection, we analyze the convergence of the pressure signals with respect to the ratio R/L and we specify the distance at which the coupling between CFD and propagation becomes valid. The sonic boom signature convergence is also studied. Finally, the acoustic signals of each geometry are compared.

In the results description, we do not provide the physical values obtained for the drag, the mid-field pressure signals and the sonic booms for confidentiality reason. We will only provide relative values scaled on the results obtained for the low drag jet.

4.1. Study parameters

The same simulation parameters are considered for the three SSBJ geometries. The flight conditions are a supersonic cruise speed of Mach 1.6 at an altitude of 13,680 m (45,000 feet). In order to be able to compare the sonic boom associated with each jet, it is fundamental to perform the computations at the same lift. Indeed, the sonic boom is a consequence of the lift effect. In this study, the cruise lift has been set to $C_l = 0.115$ by Dassault Aviation. The angle of attack for each aircraft is then set such that this lift is attained. In each case, the angle of attack of the simulation is defined on the initial mesh which is accurate close to the aircraft. These initial meshes are composed of almost 330,000 vertices for the low drag jet and 550,000 vertices for the low boom jets. The obtained angles of attack for each aircraft are near to 3 degrees.

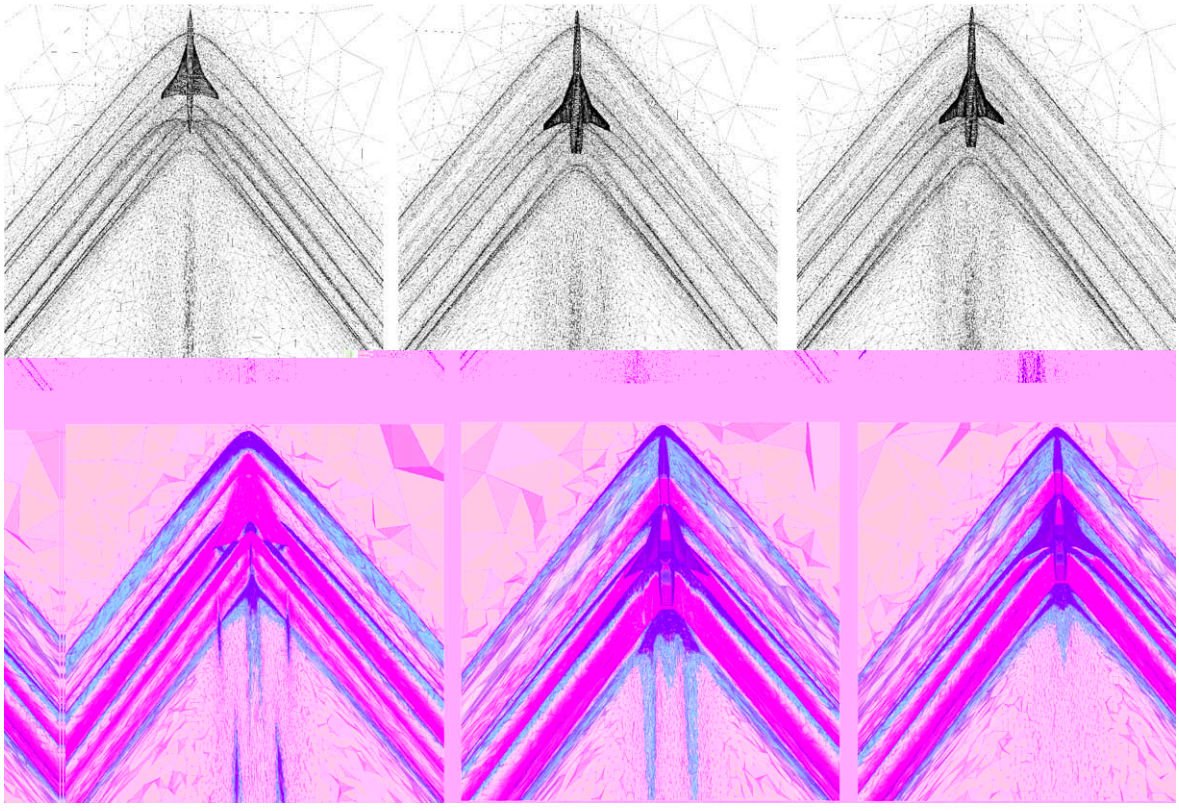

Fig. 19. From top to bottom, the low drag jet, the low boom jet and the low boom + dihedral jet. Left, view of the adapted volume mesh through the cut plane along 0*xy*, and right, the associated local Mach number iso-values.

As regards the finite volume solver, we have specified the HLLC Riemann solver, the V6-scheme with the Dervieux limiter and for the temporal integration the 5-stage order-2 SSPRK scheme. For the low boom jets, the engine data for the boundary conditions have been specified by Dassault Aviation. The lift and drag coefficient are computed according to the reference data of each geometry.

The multi-scales mesh adaptation considers a control of the interpolation error in L^2 norm of the local Mach number. The local Mach number has been selected as it is really representative of supersonic flows. We have deliberately chosen to do not adapt the aircrafts surface meshes. Indeed, the provided surface meshes are very accurate and are of high quality for the computations. A mesh gradation of 2.5 has been set [1]. A total of 32 adaptations have been performed. The mesh adaptation loop is split into 4 steps of 8 adaptations. At each step, the pair mesh-solution is algorithmically converged at a fixed complexity. This complexity is multiplied by two between two steps. This strategy has two main advantages. First, it enables us to perform a convergence study of the whole solution as a series of pair mesh-solution with an increasing accuracy is obtained. Second, considering an increasing dynamic complexity level accelerates the convergence of the whole process. We have fixed the following complexities:

$$[100,000, 200,000, 400,000, 800,000],$$

which give meshes the size of which is almost 0.8,1.7,4 and 9 million of vertices. The sizes of the final meshes are summarized in Table 4.

The simulations were run on a eight-processors 64-bits Mac Pro with an Intel Core 2 chipsets with a clock speed of 2.8 GHz with 16 Gb of RAM. The total CPU time for these simulations is approximately one week. These simulations seem to be expensive as compared to Section 2.3.2, but the accuracy and the problem scale are different, and the convergence analysis requires to fully converge the solution between each step of the adaptive loop.

4.2. Computations validation

To validate the CFD computations, the solution global convergence order for each geometry is analyzed with respect to a reference solution. In each case, the reference solution is the final solution obtained on the finest adapted mesh for a complexity equal to 800,000. The convergence is computed in L^2 norm on the local Mach number which is the variable used for

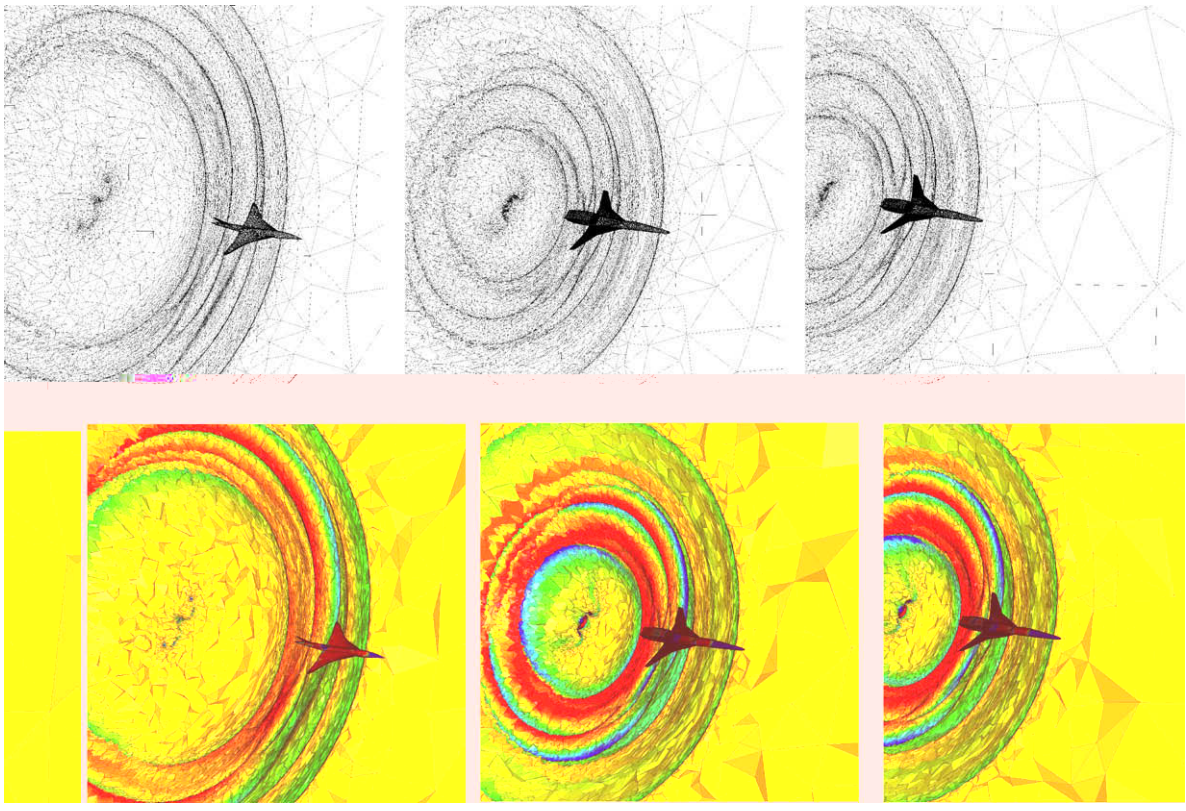

Fig. 20. From top to bottom, the low drag jet, the low boom jet and the low boom + dihedral jet. Left, view of the adapted volume mesh through the cut plane along 0*yz*, and right, the associated local Mach number iso-values.

the mesh adaptation. For the low drag, the low boom and the low boom + dihedral jets, we obtained convergence orders equal to 2, 1.5 and 1.7, respectively. The convergence plots are given in Fig. 15.

For the simplest geometry, the low drag aircraft, the theoretical order has been attained. As regards the low boom geometries, the obtained convergence order is less than two. Two hypothesizes are envisaged to explain these results. First, the final solutions for the last three steps (*i.e.*, at adaptations 16, 24 and 32) are not numerically fully converged in the adaptive process. Indeed, these geometries are really more complex than the low drag one, notably engine boundary conditions are employed. The second hypothesis is that there is a loss of convergence order due to the mesh gradation procedure. But, these hypothesizes still have to be verified.

4.3. Near-field and mid-field results

For each computation, very accurate results in the whole computational domain are obtained for the final adapted meshes containing almost 9 million vertices. In particular, the accuracy of the tetrahedral meshes has reached the surface meshes accuracy and the refinements have been propagated in the whole computational domain. This is illustrated in Fig. 16 where the Mach cones of the low boom + dihedral and the low drag SSBJs are depicted. These results point out that the numerical dissipation of the flow solver has been drastically reduced thanks to the anisotropic mesh adaptation. The

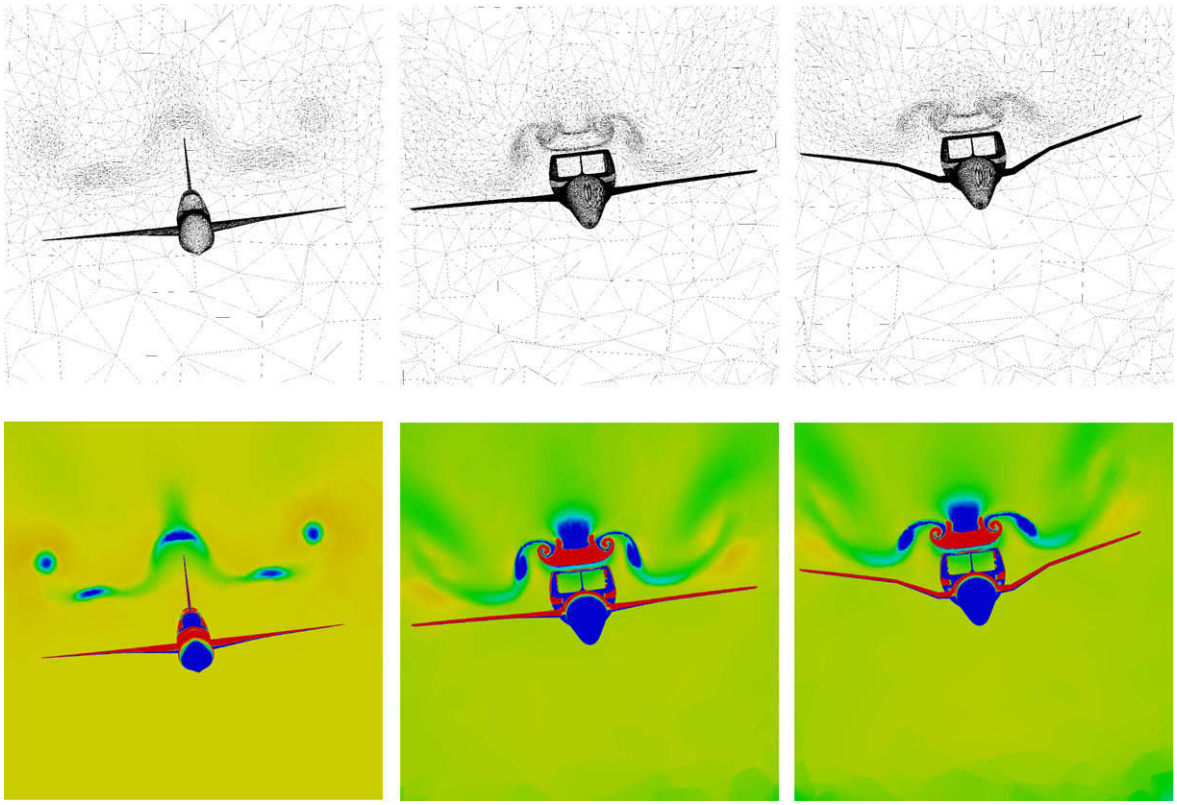

Fig. 21. From top to bottom, the low drag jet, the low boom jet and the low boom + dihedral jet. Left, view of the adapted volume mesh through the cut plane along 0*xy*, and right, the associated local Mach number iso-values.

Table 5
Mean and maximal anisotropic ratio and quotient for the three final adapted meshes reported in Table 4.

	Low drag	Low boom	Low boom + dihedral
Mean ratio	402	371	372
Max ratio	62,664	32,903	152,981
Mean quotient	57,741	48,309	49,051
Max quotient	2,710,467,666	537,166,499	465,141,987

shock waves have been accurately propagated in the whole computational domain, more than one kilometer below the SSBJs.

The surface meshes and the associated solutions for each SSBJ are shown in Fig. 17. One can see the difference in the shock position on the wing due to the wing dihedral angle for the low boom configurations. The Fig. 18 illustrates the local Mach number iso-values and the final adapted mesh in the symmetry plane 0*xz*. We notice that the shock waves and the anisotropic refinements have been propagated in the whole domain without any dissipation. We also remark the very accurate capture inside the mesh of the shock waves at the inlet and the exhaust of the engines. This points out the multi-scales behavior of the mesh adaptation approach. Cut planes of the volume meshes under the SSBJs are presented in Fig. 19. This view shows that each element of the geometry emits its own shock waves. The focalization of shocks during their propagation is also illustrated inside the mesh. Figs. 20 and 21 are two views of the final mesh and the final solution for each configuration in a cut plane behind the jet orthogonally to its path. They illustrate the mesh anisotropy along shocks and the multi-scales effects with the capture of vortices in the wake. They also point out the great complexity of the physical phenomenon and of the mesh refinement. This demonstrates the necessity to use a fully automatic mesh adaptive method.

4.4. About the meshes anisotropy

We present the amount of anisotropy obtained with the automatic mesh adaptation platform for the three simulations. The anisotropy is quantified by the anisotropic ratios and the anisotropic quotients, as explained in Section 2.2.3. The mean and the maximal values of these quantities for the three final adapted meshes are reported in Table 5. An average anisotropic ratio of almost 400 is obtained for all cases while the maximal stretching can be of the order of 10^5. The mean anisotropic quotient is a measure that evaluates the overall mesh complexity reduction achieved by the anisotropic meshes as compared to an isotropic adapted one. The mean anisotropic quotient for each simulation is almost 50,000 which is colossal.

Detailed histograms of the anisotropic ratio and quotient for the low boom + dihedral final meshes are given in Table 6. They show that the distribution of these quantities is a gaussian centered on the mean value and they confirm the highly anisotropy reached with the proposed automatic adaptive approach.

4.5. Mid-field and sonic boom convergence

Figs. 22–24 display on the left the pressure signatures for the near-field ($R/L = 1$) and the mid-field (R/L from 5 to 19) for each configuration and, on the right, the associated sonic boom signal, *i.e.,* the boom issued from those pressure signatures. In the following, we will designate by mid-field the pressure signature for R/L from 1 to 19. The mid-field signatures represent

Table 6
Anisotropic ratio (left) and quotient (right) histograms for the low boom + dihedral final adapted mesh composed of 53,884,863 tetrahedra. For each interval, the number of tetrahedra is given with the corresponding percentage.

	Low boom + dihedral (%)	
Anisotropic ratio		
$1 < \text{ratio} \leqslant 2$	38,740	0.07
$2 < \text{ratio} \leqslant 3$	175,929	0.33
$3 < \text{ratio} \leqslant 4$	274,955	0.51
$4 < \text{ratio} \leqslant 5$	328,501	0.61
$5 < \text{ratio} \leqslant 10$	1,554,625	2.89
$10 < \text{ratio} \leqslant 50$	6,620,533	12.29
$50 < \text{ratio} \leqslant 100$	5,983,308	11.10
$100 < \text{ratio} \leqslant 1000$	34,830,344	64.64
$10^3 < \text{ratio} \leqslant 10^4$	4,077,796	7.57
$10^4 < \text{ratio} \leqslant 10^5$	131	0.00
$10^5 < \text{ratio}$	1	0.00
Anisotropic quotient		
$1 < \text{quo} \leqslant 2$	10,042	0.02
$2 < \text{quo} \leqslant 3$	50,171	0.09
$3 < \text{quo} \leqslant 4$	81,027	0.15
$4 < \text{quo} \leqslant 5$	100,385	0.19
$5 < \text{quo} \leqslant 10$	526,474	0.98
$10 < \text{quo} \leqslant 50$	1,989,374	3.69
$50 < \text{quo} \leqslant 100$	1,204,384	2.24
$100 < \text{quo} \leqslant 1000$	7,408,172	13.75
$10^3 < \text{quo} \leqslant 10^4$	14,595,766	27.09
$10^4 < \text{quo} \leqslant 10^5$	20,999,034	38.97
$10^5 < \text{quo} \leqslant 10^6$	6,790,336	12.60
$10^6 < \text{quo}$	129,698	0.24

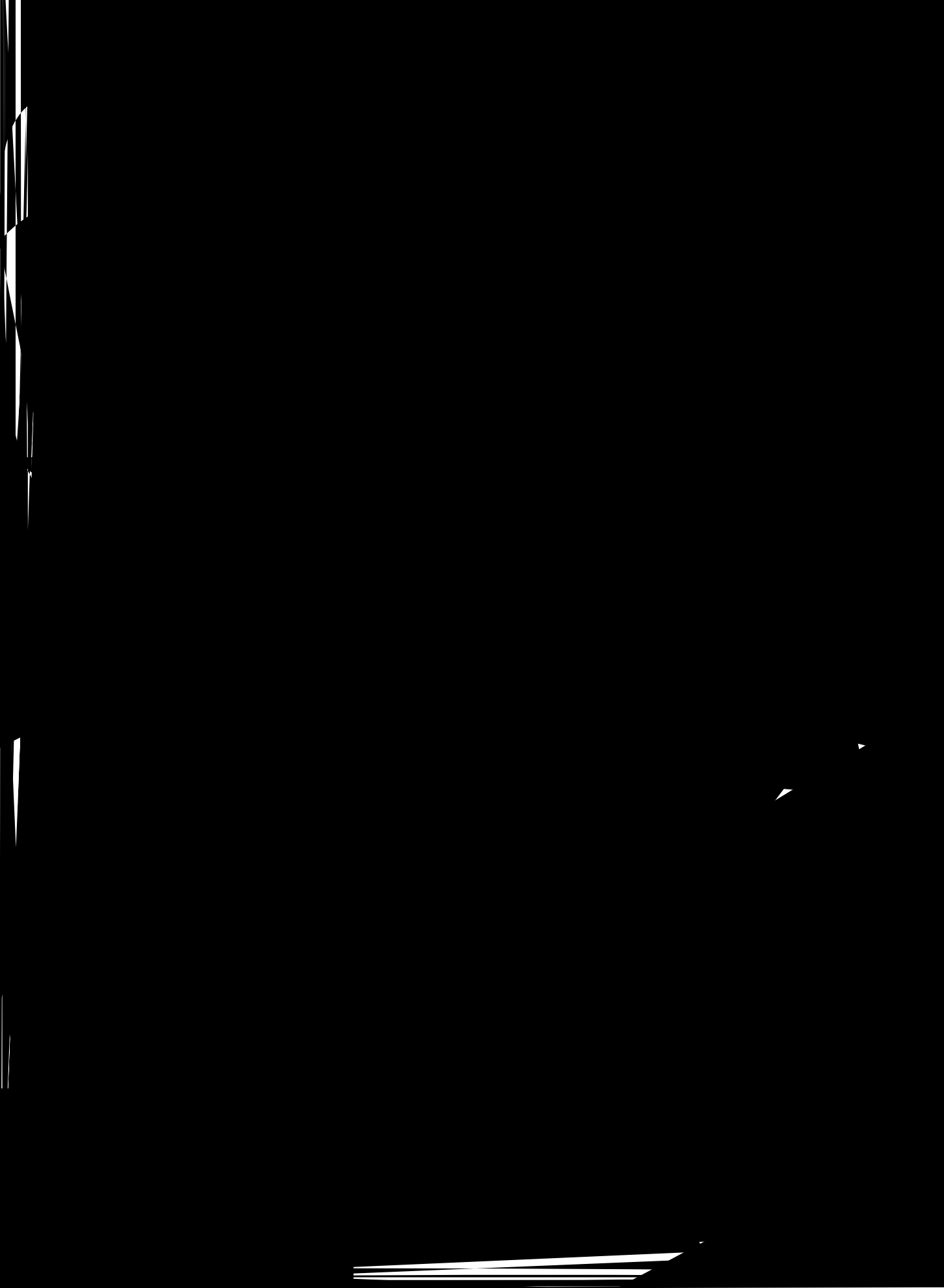

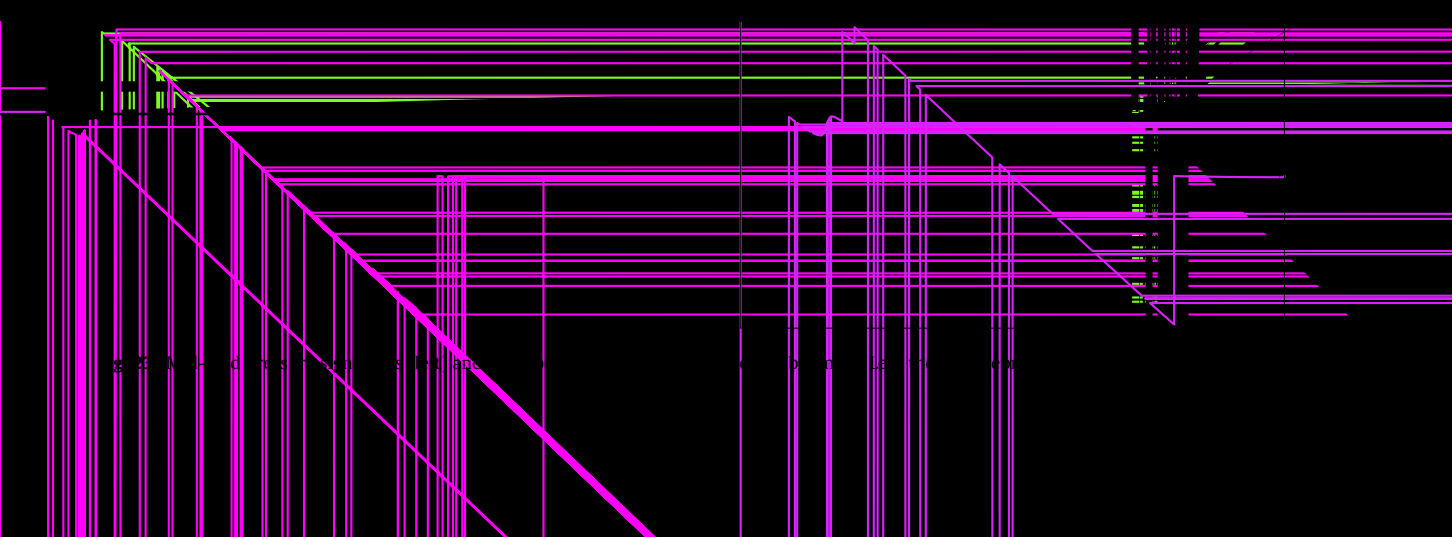

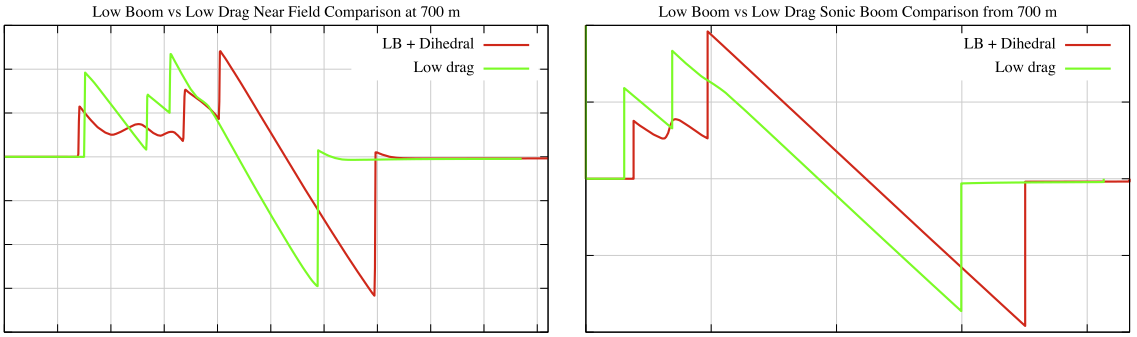

Fig. 25. Comparison of the pressure signals and the sonic booms of the low drag and the low boom + dihedral jets.

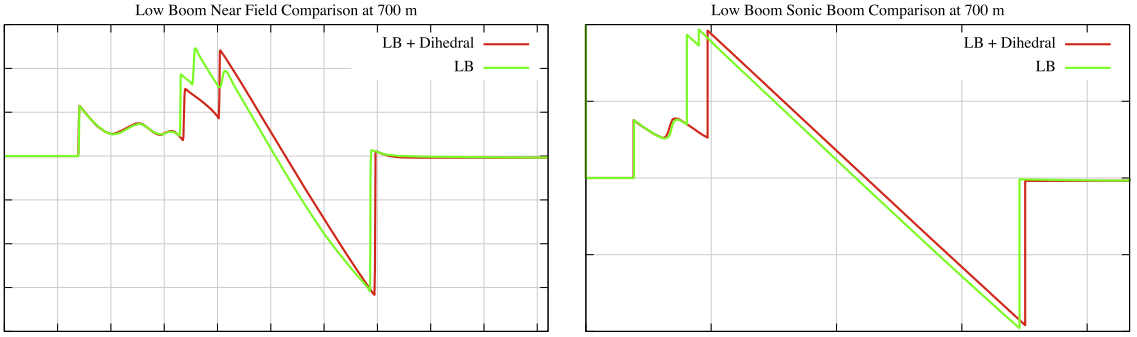

Fig. 26. Comparison of the pressure signals and the sonic booms of the low boom + dihedral and the low boom jets.

To handle these comparisons, the values of interest (the drag and the intensity of the three shocks of the boom) are given relatively to the low drag configuration. We set a drag of 1 for the low drag jet and all sonic boom shock amplitude are compared relatively to the first shock of the boom of the low drag jet which is set to an amplitude of 1. The relative results are summarize in Table 7.

We first compare the low drag and the low boom configurations, Fig. 25. Then, we analyze the effect of a wing dihedral angle on the sonic boom, Fig. 26.

4.6.1. Low drag vs. low boom + dihedral

The mid-field analysis at 700 m under the SSBJs shows that the low boom shapes reduce significantly the shock due to the nose. On the other hand, the wings shock and the tail shock are slightly higher than those of the low drag jet. These mid-field differences results in a reduction of 36% of the first shock intensity and an increase of 37% and 11% of the amplitude of the second and the third shock for the sonic boom signature. It is surprising to get an increase of 37% of the second shock intensity whereas the mid-field region associated with the wings is quite similar. As regards the shock amplitude increases for the last two shocks, it is important to recall that the low drag jet has no engines that have a notable impact on the sonic boom.

It is interesting to remark the existence of a sinusoidal region between the first and the second shock in the low boom jets sonic boom signatures. It is unusual to see such smooth regions in booms. The current analysis cannot quantify its real impact on the sonic boom. Does it increase the rise time of the second shock knowing that the rise time influence our perception of the sonic boom?

4.6.2. Wing dihedral effect

The dihedral angle of the wings intrinsically modifies the wings shocks in the mid-field. With this geometry modification, some of lift effects are sent laterally. In the pressure signature at 700 m, cf. Fig. 26, a double shock is obtained with the dihedral instead of a "three-pick" shock. The impact on the sonic boom is to shift the second shock on the right, *i.e.*, it arrives later, and to slightly reduce the amplitude of the last shock: 1.62 instead of 1.65. This is due to the effective length of the low boom + dihedral jet that has been slightly increase thanks to the dihedral. As regards the second shock, the maximal pressure has been a little reduced with the dihedral effect. However, because of the smooth sinusoidal region before the second shock, the relative amplitude is higher with the dihedral effect, 1.18 instead of 0.99, as the foot of the shock is at a lower pressure. To sum up, the dihedral effect is positive but it has a slight influence on softening the sonic boom.

In compensation, the reduction of the first shock of the boom leads to a large augmentation of the drag. A drag of 1.64 and 1.67 are obtained for the low boom and the low boom + dihedral configurations, respectively. This represents an increase of more than 60% illustrating the significant negative impact of a sonic boom optimization on the drag. Nevertheless, the drag of the low drag SSBJ is underestimated as the geometry is not supplied with engines.

5. Concluding remarks

A high-fidelity sonic boom modeling, coupling adaptive CFD mid-field simulation and ray tracing algorithm for the far-field, has been presented. A crucial point was the use of an adequate anisotropic mesh adaptation approach in order to have a valid coupling by propagating the mid-field signal far enough from the aircraft and to be able to certify the computation by attaining the theoretical mesh convergence order of the solution.

This technology illustrates that CFD on unstructured meshes is no more limited to $R/L = 1$ and that it is now possible to perform accurate simulations up to $R/L = 20$ and even more.

This approach has been validated on two test cases by comparison to experimental data and has been applied successfully to three realistic aircraft configurations. The method was able to propagate anisotropic mesh refinement in whole computational domain without any difficulties to preserve the solution accuracy. It has been demonstrated numerically that, in this case, a mid-field extraction more than $R/L = 10$ (depending on the aircraft geometry complexity) are required to obtain a precise sonic boom signature. Moreover, it has been pointed out that a consistent numerical dissipation is obtained with the flow solver on highly anisotropic adapted meshes. It results that even with smaller mesh size the sonic boom signal properties are preserved. This authorizes accurate sonic boom prediction with meshes composed of "only" 2 million vertices. This method can fast, *i.e.*, a couple of hours on a PC, provide accurate solution at moderate R/L which is of main interest for optimization platform. On the other hand, it can also be used to perform convergence studies and to assess CFD computations at large R/L with longer runs.

The proposed method can be even more improved in terms of CPU efficiency.

This adaptive procedure can be integrated in a three-stage modeling using the multi-pole reconstruction. Indeed, the multi-pole approach reduces the matching distance by taking into account crossflow effects. The adaptive CFD is then able to provide an even more accurate and certified mid-field signal (at a reduced matching distance) all around the aircraft. Moreover, this approach give another possible way to certify that there is no more non-linearities and to ensure that the coupling is valid. With this coupling, we can envisage to match mid-field CFD signals with the mid-field signals resulting from the propagation of near-field entries.

As regards the mesh adaptive technique, as the error estimate is geometric, the multi-scales mesh adaptation adapts the mesh in the whole computational domain and the mesh accuracy is related to the phenomena intensity. We can expect large improvement by considering a goal oriented approach which is under study [24]. In this case, only regions of interest for the functional will be refined and the mesh accuracy will be related to the functional accuracy thanks to the adjoint state. We thus expect enhancement in terms of accuracy and mesh size reduction.

Acknowledgments

This work was partly supported by EC DG-XIII under HISAC project.

Dassault-Aviation is gratefully acknowledged for providing the three SSBJ configurations.

We also acknowledge M.J. Aftosmis and M. Wintzer for providing the NASA model 4 geometry with the experimental data.

References

[1] F. Alauzet, Size gradation control of anisotropic meshes, Finite Elem. Anal. Des. (2009), doi:10.1016/j.finel.2009.06.028.
[2] F. Alauzet, A. Loseille, A. Dervieux, P.J. Frey Multi-dimensional continuous metric for mesh adaptation, in: Proceedings of the 15th International Meshing Roundtable, Springer, 2006, pp. 191–214.
[3] P. Batten, N. Clarke, C. Lambert, D.M. Causon, On the choice of wavespeeds for the HLLC riemann solver, SIAM J. Sci. Comput. 18 (6) (1997) 1553–1570.
[4] H.W. Carlson, Simplified sonic-boom prediction, TP, 1122, Nasa, 1978.
[5] H.W. Carlson, R.J. Mack, O.A. Morris, A wind-tunnel investigation of the effect of body shape on sonic-boom pressure distributions, TN, D-3106, Nasa, 1965.
[6] M.J. Castro-Díaz, F. Hecht, B. Mohammadi, O. Pironneau, Anisotropic unstructured mesh adaptation for flow simulations, Int. J. Numer. Meth. Fluids 25 (1997) 475–491.
[7] Ph. Clément, Approximation by finite element functions using local regularization, Revue Française d'Automatique Informatique et Recherche Opérationnelle R-2 (1975) 77–84.
[8] P.-H. Cournède, B. Koobus, A. Dervieux, Positivity statements for a Mixed-Element-Volume scheme on fixed and moving grids, Eur. J. Comput. Mech. 15 (7–8) (2006) 767–798.
[9] C. Debiez, A. Dervieux, Mixed-element-volume MUSCL methods with weak viscosity for steady and unsteady flow calculations, Computer and Fluids 29 (2000) 89–118.
[10] C. Dobrzynski, P.J. Frey, Anisotropic Delaunay mesh adaptation for unsteady simulations, in: Proceedings of the 17th International Meshing Roundtable, Springer, 2008, pp. 177–194.
[11] P.J. Frey, F. Alauzet, Anisotropic mesh adaptation for CFD computations, Comput. Methods Appl. Mech. Eng. 194 (48-49) (2005) 5068–5082.
[12] P.J. Frey, P.-L. George, Mesh Generation, second ed., Application to Finite Elements, ISTE Ltd. and John Wiley & Sons, 2008.
[13] A.R. George, Reduction of sonic boom by azimuthal redistribution of overpressure, AIAA Journal 7 (2) (1969) 291–298.

[14] P.-L. George, Tet meshing: construction, optimization and adaptation, in: Proceedings of the 8th International Meshing Roundtable, South Lake Tao, CA, USA, 1999.
[15] C. Gruau, T. Coupez, 3D tetrahedral, unstructured and anisotropic mesh generation with adaptation to natural and multidomain metric, Comput. Methods Appl. Mech. Eng. 194 (48-49) (2005) 4951–4976.
[16] W.D. Hayes, R.C. Haefeli, H.E. Kulsrud. Sonic boom propagation in a stratified atmosphere with computer program, TN. CR-1299, Nasa, 1969.
[17] N. Héron, F. Coulouvrat, F. Dagrau, G. Rogé, Z. Johan. Hisac midterm overview of sonic boom issues, in: Proceedings of the 19th international congress on acoustics-ICA, Madrid, Spain, 2007.
[18] W. Huang, Metric tensors for anisotropic mesh generation, J. Comput. Phys. 204 (2) (2005) 633–665.
[19] L.W. Hunton, R.M. Hicks, J.P. Mendoza, Some effects of wing planform on sonic boom, TN. D-7160, Nasa, 1973.
[20] ICAO, Manual of the ICAO Standard Atmosphere (extended to 80 kilometres). Doc 7488, third edition, 1993.
[21] W.T. Jones, E.J. Nielsen, M.A. Park, Validation of 3d adjoint based error estimation and mesh adaptation for sonic boom reduction, AIAA Paper (2006) 1150–2006.
[22] B. Van Leer, Towards the ultimate conservative difference scheme I. The quest of monotonicity, Lecture Notes in Physics 18 (1972) 163.
[23] X. Li, M.S. Shephard, M.W. Beal, 3D anisotropic mesh adaptation by mesh modification, Comput. Methods Appl. Mech. Eng. 194 (48-49) (2005) 4915–4950.
[24] A. Loseille. Adaptation de maillage anisotrope 3D multi-échelles et ciblée à une fonctionnelle pour la mécanique des fluides, Application à la prédiction haute-fidélité du bang sonique, Ph.D. Thesis, Université Pierre et Marie Curie, Paris VI, Paris, France, 2008, (in French).
[25] A. Loseille, F. Alauzet, Continuous mesh model and well-posed continuous interpolation error estimation, RR-6846, INRIA, March 2009.
[26] A. Loseille, A. Dervieux, P.J. Frey, F. Alauzet, Achievement of global second-order mesh convergence for discontinuous flows with adapted unstructured meshes, AIAA Paper (2007) 2007–4186.
[27] J.A. Page, K.J. Plotkin, An efficient method for incorporating computational fluid dynamics into sonic boom prediction, AIAA Paper (1991) 1991–3275.
[28] C. C Pain, A.P. Humpleby, C.R.E. de Oliveira, A.J.H. Goddard, Tetrahedral mesh optimisation and adaptivity for steady-state and transient finite element calculations, Comput. Methods Appl. Mech. Eng. 190 (2001) 3771–3796.
[29] Pederson, Sonic boom technologies and challenges, in: FAA Civil Supersonic Aircraft Workshop, Arlington, VI, USA, 2003.
[30] K.J. Plotkin, Theoretical basis for the finite difference extrapolation of sonic boom signatures, in: NASA Conference Publication 3335, vol. 1, 1995, pp. 54–67.
[31] K.J. Plotkin, J.A. Page, Extrapolation of sonic boom signatures from CFD solutions, AIAA Paper (2002) 2002-0922.
[32] P. Roe, Approximate Riemann solvers, parameter vectors, and difference schemes, J. Comput. Phys. 43 (1981) 357–372.
[33] C.W. Shu, S. Osher, Efficient implementation of essentially non-oscillatory shock-capturing schemes, J. Comput. Phys. 77 (1988) 439–471.
[34] R.J. Spiteri, S.J. Ruuth, A new class of optimal high-order strong–stability–preserving time discretization methods, SIAM J. Numer. Anal. 40 (2) (2002) 469–491.
[35] J.L. Steger, R.F. Warming, Flux vector splitting of the inviscid gas dynamic equations with application to finite-difference methods, J. Comput. Phys. 40 (1981) 263–293.
[36] A. Tam, D. Ait-Ali-Yahia, M.P. Robichaud, M. Moore, V. Kozel, W.G. Habashi, Anisotropic mesh adaptation for 3D flows on structured and unstructured grids, Comput. Methods Appl. Mech. Eng. 189 (2000) 1205–1230.
[37] Ch. Thomas, Extrapolation of sonic boom pressure signatures by the waveform parameter method, TN. D-6832, Nasa, 1972.
[38] K.A. Waithe, Application of USM3D for sonic boom prediction by utilizing a hybrid procedure, AIAA Paper (2008) 2008-129.
[39] M. Wintzer, M. Nemec, M.J. Aftosmis, Adjoint-based adaptive mesh refinement for sonic boom prediction, AIAA Paper (2008) 2008-6593.